



1 **Orbitally forced environmental changes during the accumulation**  
2 **of a Pliensbachian (Lower Jurassic) black shale in northern Iberia**

3 Naroa Martínez-Braceras<sup>1,2</sup>; Aitor Payros<sup>1</sup>; Jaume Dinarès-Turell<sup>3</sup>; Idoia Rosales<sup>4</sup>; Javier  
4 Arostegi<sup>1</sup> and Roi Silva-Casal<sup>5</sup>

5 <sup>1</sup> Department of Geology, Faculty of Science and Technology, University of the Basque  
6 Country (UPV/EHU), P.O. Box 644, 48080 Bilbao, Spain

7 <sup>2</sup> Laboratorio de Evolución Humana, Departamento de Historia, Geografía y  
8 Comunicación, Universidad de Burgos, Edificio I+D+I, Plaza de Misael Bañuelos/n,  
9 09001 Burgos, Spain

10 <sup>3</sup> Istituto Nazionale di Geofisica e Vulcanologia, Via di Vigna Murata 605, 00142 Rome,  
11 Italy

12 <sup>4</sup> Centro Nacional Instituto Geológico y Minero de España (IGME, CSIC), La Calera 1,  
13 Tres Cantos, 28760 Madrid, Spain

14 <sup>5</sup> Dpto. Dinàmica de la Terra i de l'Oceà, Facultat de Ciències de la Terra, UB. 08028  
15 Barcelona.

16 Correspondence to: Naroa Martínez Braceras ([naroa.martinez@ehu.eus](mailto:naroa.martinez@ehu.eus))

17 **Abstract**

18 Lower Pliensbachian hemipelagic successions from the north Iberian palaeomargin are  
19 characterized by the occurrence of organic-rich calcareous rhythmites of decimetre-thick  
20 limestone and marl beds and thicker black shale intervals. Understanding the genetic  
21 mechanisms of the cyclic lithologies and involved processes along with the nature of the  
22 carbon cycle is of primary interest. The cyclostratigraphic study carried out in one of the  
23 black shales exposed in Santiurde de Reinosa (Basque-Cantabrian Basin) revealed that  
24 the calcareous rhythmites responded to periodic environmental variations in the  
25 Milankovitch-cycle band, with the prevalence of precession, short eccentricity and long  
26 eccentricity cycles.

27 The main environmental processes that determined the formation of the rhythmite were  
28 deduced on the basis of the integrated sedimentological, mineralogical and geochemical  
29 study of an eccentricity bundle. The formation of precession couplets was controlled by  
30 variations in carbonate production and dilution by terrigenous supplies, along with  
31 periodic changes in bottom water oxygenation. Precessional configurations with marked  
32 annual seasonality, increased terrigenous input (by rivers or wind) to marine areas and  
33 boosted organic productivity in surface waters. The great accumulation of organic matter  
34 on the seabed eventually decreased bottom waters oxygenation, which might also be  
35 influenced by reduced ocean ventilation. Thus, deposition of organic-rich marls and  
36 shales occurred when annual seasonality was maximum. On the contrary, a reduction in  
37 terrestrial inputs at precessional configurations with minimal seasonality diminished



38 shallow organic productivity, added to an intensification of vertical seawater mixing,  
39 contributed to increasing the oxidation of organic matter. These conditions also favoured  
40 greater production and basinward exportation of carbonate mud in shallow marine areas,  
41 causing the formation of limy hemipelagic beds. Short eccentricity cycles modulated the  
42 amplitude of precession driven variations in terrigenous input and oxygenation of bottom  
43 seawaters. Thus, the amplitude of the contrast between successive precessional beds  
44 increased when the Earth's orbit was elliptical and diminished when it was circular. The  
45 data also suggest that short eccentricity cycles affected short-term sea level changes,  
46 probably through orbital modulated aquifer-eustasy.

## 47 **1. Introduction**

48 As a consequence of the gravitational interaction between astronomical bodies, the  
49 Earth's axial orientation and orbit vary cyclically at timescales that range from tens of  
50 thousands to few million years (Berger and Loutre, 1994). These variations in orbital  
51 configuration regulate the latitudinal distribution of solar radiation (insolation), which  
52 determines the contrast between seasons. These periodic changes in the climatic system  
53 can be recorded as cyclic stratigraphic successions, the so-called rhythmites, in a wide  
54 range of sedimentary environments (Einsele and Ricken, 1991). As the open ocean is  
55 hardly affected by processes that may interrupt the continuous settling of fine-grained  
56 particles or erode the seabed, deep marine pelagic sediments accumulate at a generally  
57 constant, but slow (few cm/ky), sedimentation rate. Thus, pelagic rhythmites from both  
58 oceanic sediment cores and indurate successions contain accurate records of orbitally  
59 modulated, quasi-periodic climate-change episodes, which provide high-resolution  
60 astrochronologies (Hinnov, 2013).

61 Significant progress in Early Jurassic cyclostratigraphy has been made in the last few  
62 decades thanks to the study of exceptional orbitally modulated sedimentary records  
63 obtained from deep marine environments of the Perytethyan realm (e.g., Cardigan and  
64 Cleveland Basins by Hüsing et al., 2014, Storm et al., 2020; Pieńkowski et al., 2021; Paris  
65 Basin by Charbonnier et al., 2023). Although these studies provided relevant  
66 astrochronological information, they did not focus on the climatic and environmental  
67 impact of the orbital cycles on the sedimentary record. Other studies deduced a control of  
68 long-term orbital cycles on the Jurassic carbon cycle (Martinez and Dera, 2015; Ikeda et  
69 al., 2016; Hollar et al 2021; Zhang et al., 2023), but the climatic and environmental  
70 influence of short-term cycles has been less studied (Hinnov and Park, 1999; Ikeda et al.,  
71 2016; Hollar et al., 2023).

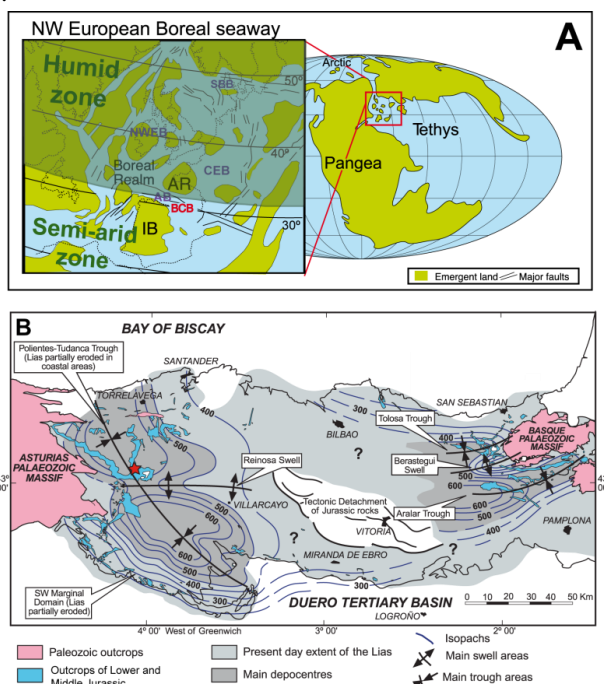
72 The aim of this study was to analyze the climatic and environmental impact of short-term  
73 astronomical cycles on Lower Jurassic deep marine deposits. To this end, a hemipelagic  
74 alternation of limy and marl/shale beds was analyzed in the Santiurde de Reinosa section  
75 (hereafter referred to as the Santiurde section), Basque-Cantabrian Basin (BCB),  
76 Cantabria province, Spain. In order to determine if sedimentation was orbitally forced, a  
77 cyclostratigraphic analysis of the hemipelagic rythmites was firstly undertaken.  
78 Subsequently, an integrated multiproxy study was performed in a selected interval of the



79 section in order to disentangle what sedimentary processes and environmental factors  
80 influenced on the formation of the hemipelagic rhythmites.

## 81 2. Geological setting

82 In early Jurassic times the BCB was located to the south of Armorican and to the north of  
83 the Iberian Massif, being part of the Laurasian epicontinental seaway which connected  
84 the Boreal Sea with the southern Tethyan Ocean (Fig. 1A; Aurell et al., 2002; Rosales et  
85 al., 2004). Previous palaeogeographic reconstructions located the north Iberian margin at  
86 approximately 30°N palaeolatitude (Quesada et al., 2005; Osete et al., 2010). Hence, the  
87 source area was located in the semiarid belt but close to the boundary with the humid  
88 climatic zone (temperate climate characterized by megamonsoons; Dera et al., 2009;  
89 Deconinck et al., 2020), which made it especially sensitive to astronomically driven  
90 climate change.



91 Figure 1. A) Palaeogeography and climatic zonation (modified from Quesada et al., 2005; Dera et al., 2009; Ostete et  
92 al., 2010) of Western Europe in Early Jurassic times. IB: Iberian massif, AR: Armorican massif, AB: Asturian Basin,  
93 BCB: Basque-Cantabrian Basin, CEB: Central European Basin, NWEB: NW European Basin, SBB: South Boreal  
94 Basin. B) Simplified geographic and geological map of lower and middle Jurassic outcrops in the BCB area, with  
95 location of the studied Santurde section (red star). Superimposed isopach map shows the thickness of the lower Jurassic  
96 rocks and the basin configuration in sedimentary troughs and swells (modified from Quesada et al., 2005).  
97

98 Hettangian and lower Sinemurian deposits accumulated in evaporitic tidal flats and  
99 shallow carbonate ramps, whereas the overlying Sinemurian-Callovian succession was  
100 accumulated in relatively deep, open marine conditions (Aurell et al., 2002; Quesada et  
101 al., 2005). Differential subsidence during the Jurassic related to early mobilization of  
102 underlying Triassic salt resulted in the creation of several troughs in the BCB (Fig. 1B,  
103 Quesada et al., 2005).



104 Pliensbachian (192.9–184.2 Ma) hemipelagic successions of the BCB (Camino  
105 Formation; Quesada et al., 2005) are characterized by the occurrence of three black shale  
106 (BS) intervals, each several tens of metres thick (Braga et al., 1988; Quesada et al., 1997,  
107 2005; Quesada and Robles 2012; Rosales et al., 2001, 2004, 2006). These BS intervals  
108 can be correlated with similar coeval deposits in neighbouring basins in Asturias (Borrego  
109 et al., 1996; Armendáriz et al., 2012; Bádenas et al., 2012, 2013; Gómez et al., 2016).  
110 Coeval organic rich marine facies have also been observed in other Thetyan lower  
111 Jurassic successions from Portugal (Silva et al., 2011), United Kindom (Hüsing et al.,  
112 2014), France (Bougeault et al., 2017) and Germany (Pieńkowski et al., 2008). The BCB  
113 Pliensbachian BS intervals present relatively high organic carbon content (2–6wt%), high  
114 pyrite concentrations and scarce benthic faunas. Thermal maturity analysis showed that  
115 the BS intervals found at the depocentres are overmature today, but they sourced the only  
116 oil reservoir discovered inland Iberia (Quesada et al., 1997, 2005; Quesada and Robles,  
117 2012; Permanyer et al., 2013). Pyrolysis of thermally immature samples from marginal  
118 areas showed total organic carbon values of up to 20 wt% and hydrogen index values up  
119 to 600–750 mg HC/g TOC (Suárez-Ruiz and Prado, 1987; Quesada et al., 1997). Analyses  
120 on organic matter (OM) showed that the assemblage is mainly composed of marine type-  
121 II kerogens, in which amorphous and algal material prevail (Quesada et al., 1997, 2005;  
122 Permanyer et al., 2013). More specifically, the analysis revealed a low content in  
123 gammaceranes, which suggests normal salinity conditions, and great abundance of  
124 trilocular triterpanes, which can be associated to *Tasmanites* type unicellular green algae  
125 with organic theca. In addition, the high content in isorenieratene byproducts, such as  
126 aryl-isoprenoids, indicates the occurrence of photosynthetic and sulfurous green algae  
127 communities (*Chlorobiaceae*) developed in oxygen-depleted conditions.

128 The Santiurde section studied herein is exposed at exit 144 of motorway A67 (UTM  
129 X411431.091 Y4769002.593; Fig. 1B), approximately 50 km south-west of Santander  
130 and 1 km north-west of a coeval section studied by others at the train station in the same  
131 locality (e.g. Rosales et al., 2001, 2004, 2006; Quesada et al., 2005), with which a bed-  
132 by-bed correlation can be readily carried out. The studied succession begins with 2.5 m  
133 of alternating grey limestones and thin marlstones (Puerto Pozazal Formation), which are  
134 overlain by 20 m of the lower part of the Pliensbachian Camino Formation, mainly made  
135 up of alternations of hemipelagic marls, limestones and overmature black shales (Rosales  
136 et al., 2004; Quesada et al., 2005). The section includes the oldest (*Uptonia jamesoni*  
137 Zone) of the BS intervals identified in the Camino Formation (Fig. 2A).

### 138 3. Materials and methods

#### 139 3.1. Cyclostratigraphic analysis of the Santiurde section

140 A detailed cm-scale stratigraphic log was measured in a 30.40 m thick succession that  
141 exposes the transition from the Puerto Pozazal Formation to the Pliensbachian Camino  
142 Formation. A broad range of sedimentological features, such as bed shape, thickness,  
143 composition, palaeontological content and structures, were annotated. A total of 373 hand  
144 samples were collected, with a resolution of at least 3 samples per bed, avoiding visible



145 skeletal components, burrows and veins. The weight normalized low-field magnetic  
146 susceptibility (MS) of the samples was measured using a Kappabridge KLY-3 instrument  
147 (Geophysika Brno) housed at the Geology department of the University of the Basque  
148 Country, Bilbao, Spain. Subsequently, rock-powder samples were obtained and stored in  
149 transparent antiglare prismatic vials, which were scanned in a dark room using a desktop  
150 office scanner. The average colour (RGB value) of the scanned images of rock-powder  
151 samples was determined using the ImageJ software and following the protocol in Dinarès-  
152 Turell et al. (2018) and Martínez-Braceras et al. (2023).

153 In order to carry out a cyclostratigraphic analysis, the Acycle software (Li et al., 2019)  
154 and the Astrochron package for R (Meyers et al., 2014) were used. The MS and colour  
155 data series were linearly interpolated and detrended first. Subsequently, power spectra  
156 were obtained using the  $2\pi$ -Multi Taper Method (MTM) with three tapers, and confidence  
157 levels (CL) were calculated following robust red-noise modelling (Mann and Lees 1996).  
158 In addition, Evolutive Harmonic Analysis (EHA; Meyers et al., 2001) and Wavelet  
159 analyses (Torrence and Compo, 1998) were also carried out in order to examine the  
160 variability of the main frequency bands throughout the succession. Finally, the most  
161 significant frequency bands identified in the data series were isolated by Gaussian  
162 bandpass filtering.

### 163 **3.2. Multiproxy analysis of Bundle 9**

164 An integrated analysis of several environmentally sensitive proxies was undertaken in the  
165 19 beds found between 20.30 and 23.85 m of the stratigraphic succession. This interval  
166 includes a complete eccentricity bundle (B9 see results below), as well as the uppermost  
167 and lowermost beds of the underlying and overlying bundles, respectively. Fifty-seven  
168 samples were collected to perform a calcimetric analysis by measuring the carbonate  
169 percentage in 1 g of powder of each sample using a FOGL digital calcimeter (BD  
170 inventions; accuracy of 0.5%) housed at the University of the Basque Country. These  
171 samples were also analysed for inorganic  $\delta^{13}\text{C}_{\text{carb}}$  and  $\delta^{18}\text{O}_{\text{carb}}$  content at the Leibniz  
172 Laboratory for Radiometric Dating and Stable Isotope Research (Kiel University,  
173 Germany) using a Kiel IV carbonate preparation device connected to a ThermoScientific  
174 MAT 253 mass spectrometer. Precision of all internal and external standards (NBS19 and  
175 IAEA-603) was better than  $\pm 0.05\text{‰}$  for  $\delta^{13}\text{C}_{\text{carb}}$  and  $\pm 0.09\text{‰}$  for  $\delta^{18}\text{O}_{\text{carb}}$ . All values are  
176 reported in the VPDB notation relative to NBS19.

177 In addition, one sample from the central part of each bed was studied for petrographic  
178 and scanning electron microscope (SEM) analysis, mineralogical content, elemental  
179 composition and organic geochemistry. For the mineralogical and geochemical analyses,  
180 the samples were ground in the laboratory. Whole-rock mineralogy was obtained by  
181 analysing randomly oriented rock powder by X-ray diffraction (XRD), using a Philips  
182 PW1710 diffractometer (Malvern Analytical, Malvern, UK) at the University of the  
183 Basque Country. The step size was  $0.02^\circ$  2h with a counting time of 0.5 s per step. Major  
184 and trace element concentrations were determined at the University of the Basque  
185 Country using a Perkin-Elmer Optima 8300 spectrometer (ICP-OES; PerkinElmer) and a



186 Thermo XSeries 2 quadrupole inductively coupled plasma mass spectrometer (ICP-MS;  
187 Thermo Fisher Scientific) equipped with a collision cell, an interphase specific for  
188 elevated total dissolved solids (Xt cones), a shielded torch, and a gas dilution system.  
189 Analysis of the JG-2 granite standard and error estimates of each element showed that the  
190 uncertainty of the results corresponds to the 95% confidence level. Finally, organic  
191 carbon ( $C_{org}$ ) and organic nitrogen ( $N_{org}$ ) contents, as well as their isotopic  $\delta^{13}C_{org}$  and  
192  $\delta^{15}N_{org}$  values were obtained by combustion of powdered and decarbonated samples in  
193 an elemental analyzer Flash EA 1112 (ThermoFinnigan) connected to a DeltaV  
194 Advantage mass spectrometer (Thermo Scientific) at the University of A Coruña, Spain.  
195 Calibration of  $^{13}C_{org}$  and  $^{15}N_{org}$  was done against certificated standards USGS 40,  
196 USGS41a, NBS 22 and USGS24. Results are expressed in the VPDB notation, accuracy  
197 (standard deviation) being  $\pm 0.15\%$ .

198 In order to explore compositional relationships and trends using comprehensive multi-  
199 elemental datasets, Pearson correlation coefficients ( $r$ ) and their significance ( $P$ -values)  
200 were estimated for pairs of variables using the SPSS 28 statistical package (IBM  
201 Corporation, SPSS statistics for Windows, version 28.0.1.1, 2022, Armonk, NY, USA).  
202 In addition, a multivariate factor analysis was undertaken with the aim of identifying the  
203 number of virtual variables (factors) that explains the highest percentage of the variability  
204 in the analyzed dataset.

## 205 **4. Results**

### 206 **4.1. General Santiurde section**

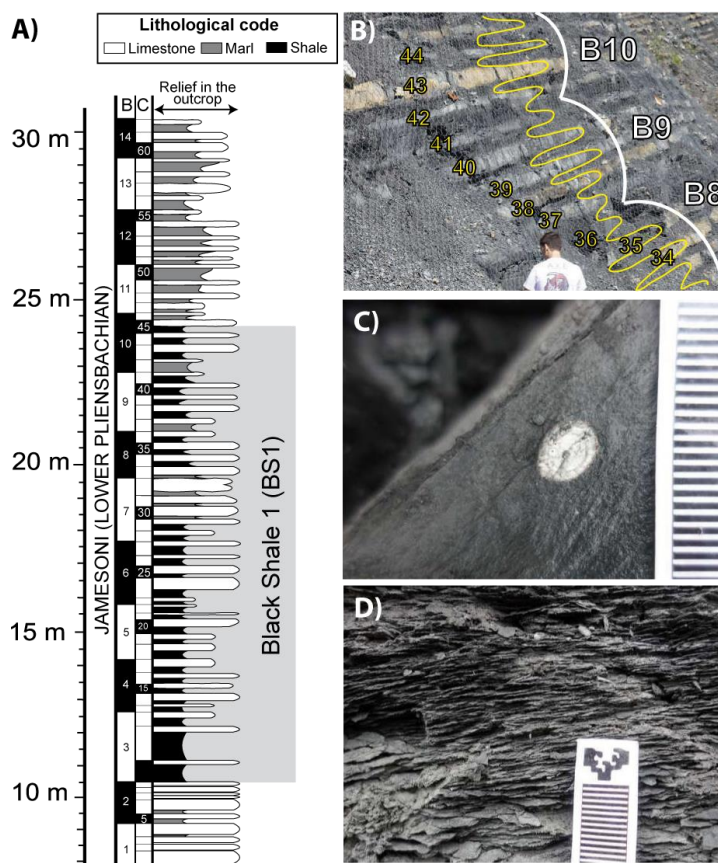
#### 207 **4.1.1. Sedimentology and petrography**

208 The succession displays an alternation of weather resistant, light coloured, bioturbated  
209 limestones or marly limestones, and weather recessive, dark coloured, laminated marls or  
210 shales (Fig. 2). In the outcrop, the fossil record of limestones and marly limestones is  
211 dominated by isolated ammonites, belemnites and brachiopods (Fig. 2C). Thin sections  
212 show mudstones and wackestones with dispersed benthic foraminifera, fragmented  
213 echinoderms, brachiopods and pyritized bivalve shells (mainly pectinids) in a microspar  
214 matrix (Figs. 3A and C). Well-preserved placoliths of coccolithophorids were identified  
215 by SEM (Figs. 3C and G).

216 Both marls and shales constitute friable, weather-recessive beds, the latter generally  
217 showing darker colour and more prominent lamination (Fig. 2D), also observed in thin  
218 sections (Fig. 3B). Furthermore, marls contain nekto-planktonic fossils (ammonites,  
219 belemnite and calcareous unicellular algae) and evidence of benthonic communities  
220 (pyritized shells of bivalves and rhynchonellid brachiopods; trace fossils, such as  
221 *Chondrites* and *Planolites*), whereas the latter are absent in shales. This is confirmed by  
222 SEM analysis, as marls contain isolated, broken and randomly oriented clay minerals that  
223 wrap well-preserved coccoliths and calcispheres with signs of bioturbation (Fig. 3C, 3D  
224 and 3G). Nektonic organisms and planktonic unicellular algae also occur in shales, but  
225 benthonic fauna and bioturbation are virtually absent. SEM observations also showed that

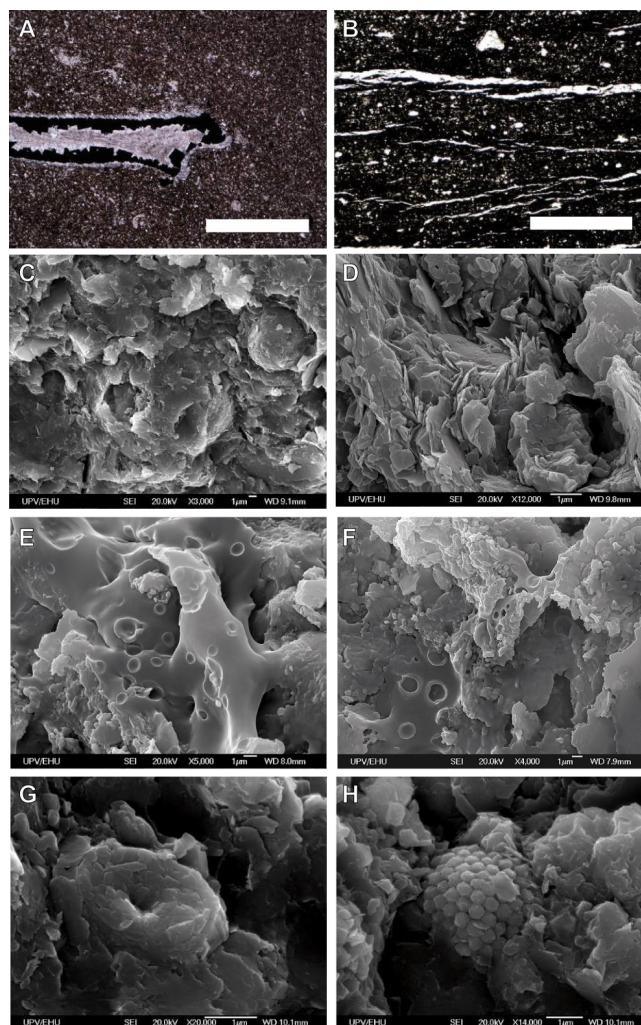


226 the lamination in shales is caused by the alternation of detrital components (mainly clays  
227 but also quartz) and organic components (such as bitumen, polymeric extracellular  
228 substances linked to biofims, filamentous bacterial mats, or fungal hyphae; Fig. 3E and  
229 3F). Pyrite fambroids are more common in shales than in limy beds (Fig. 3H).



230  
231 Figure 2. A) Synthetic lithological log of the Santiurde section, including chronostratigraphy from Quesada et al. (2005)  
232 and Rosales et al. (2006). B) Calcareous couplets (yellow numbers) of bundles 8 to 10 (white numbers) in the Santiurde  
233 outcrop. The white curve shows the relief of successive beds in the outcrop (left, weather recessive; right, weather  
234 resistant), which is mainly determined by their carbonate content. C) Close up of a marly limestone with a partly  
235 pyritized belemnite. D) Close up of a laminated black shale. Scale bar in mm.

236 A total of 62 calcareous couplets (C1 to C62) were identified in the studied succession,  
237 whose thicknesses vary from 8 to 97 cm, averaging out at 36 cm (Fig. 2A and 4). These  
238 couplets display a larger-scale arrangement in 12 complete bundles plus another two  
239 incomplete bundles at the base and top of the section. These bundles range in thickness  
240 from 126 to 208 cm (average: 167.3 cm) and are composed of four to six couplets  
241 (generally five). Bundles typically contain a package of three prominent central couplets  
242 (with significant lithological contrast between successive limestone and marl/shale beds)  
243 which is underlain and overlain by less obvious couplets (lower lithological contrast  
244 between successive marl and marly limestone beds).



245  
246 Figure 3. Petrographic views of limestone C41 (A) and shale C36 (B). The white bars represent 1 mm. C) General  
247 texture of a limestone bed (couplet C37), showing partly dissolved and broken coccoliths and calcispheres. D) General  
248 texture of a marly bed (couplet C37) with evidence of bioturbation. E) and F) probable biofilms. F) Well preserved  
249 coccolith. G) Pyrite fambroid.

#### 250 4.1.2. Colour, calcium carbonate and magnetic susceptibility

251 Colour values (mean RGB) range from 69.87 to 158.99, averaging out at 102.73 (Fig. S1;  
252 Table S1). The colour curve oscillates in line with the lithological alternation, colour  
253 values generally being higher in limestones and marly limestones (average of 115.14)  
254 than in intervening marls or shales (average of 90.71). The variations in colour values are  
255 more significant in the central couplets of bundles than at bundle boundaries. This  
256 suggests that, as shown in previous studies (Dinarès-Turell et al., 2018; Martínez-  
257 Braceras et al., 2023), colour values are representative of the carbonate content of the  
258 samples. This is confirmed by the carbonate content analysis carried out between couplets





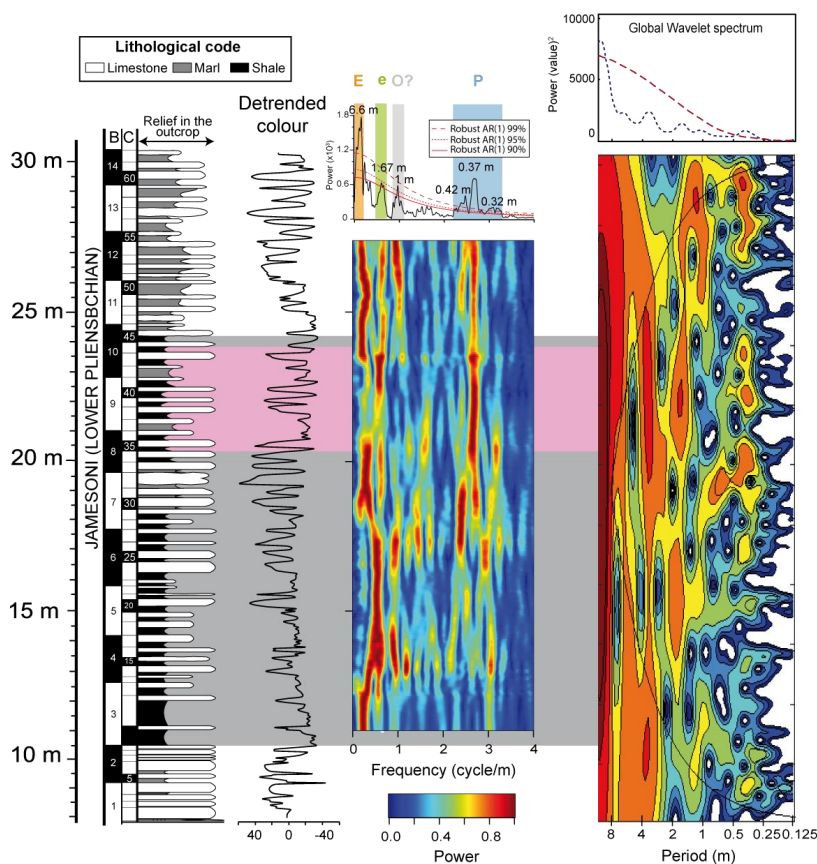
259 C35 to C44 (see below), as both colour and carbonate content show the same arrangement  
260 in couplets and bundles ( $r: 0.89, p < 0.001$ ; Fig. S1).

261 Weight-normalized magnetic susceptibility values range from  $5.08 \times 10^{-06}$  to  $1.67 \times 10^{-06}$   
262  $\text{m}^3/\text{kg}$ , averaging out at  $9.9 \times 10^{-06} \text{m}^3/\text{kg}$  (Fig. S1, Table S1). In most cases, limestones  
263 and marly limestones have higher susceptibility (average:  $1.08 \times 10^{-05} \text{m}^3/\text{kg}$ ) than shales  
264 and marls (average:  $8.99 \times 10^{-06} \text{m}^3/\text{kg}$ ). The MS of hemipelagic deposits is commonly  
265 determined by their paramagnetic components (mostly detrital clays; Kodama and  
266 Hinnov, 2015). However, in Santiurde this parameter does not show a great correlation  
267 with colour ( $r: 0.48, p < 0.001$ , all section; Fig. S1) or calcium carbonate ( $r: 0.36, p < 0.001$ ,  
268 between C35 and C44; Fig. S1). Therefore, the Santiurde relationship suggests that the  
269 MS signal is more likely controlled by ferromagnetic minerals, such as magnetite (Fig.  
270 S2).

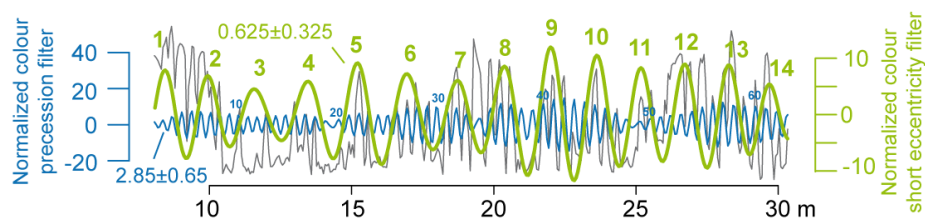
#### 271 4.1.3. Time series analysis

272 Prior to spectral analysis, the colour data series was regularly interpolated (spacing of  
273 0.06 m) and the 3<sup>rd</sup> order polynomial trend was subtracted. The  $2\pi$ -MTM power spectrum  
274 of the colour data series shows peaks at four period bands: 30-42 cm (peaking at 37 cm),  
275 1 m, 1.67 m and 5-10 m (Fig. 4). The short period band shows significant peaks above  
276 99% CL. In the intermediate period band, the 1 m peak exceeds 95% CL and the 1.67 m  
277 peak reaches 90% CL. The long period band, which peaks at 6.6 m, is above 99% CL.  
278 The short period band matches the average thickness of couplets and the longest  
279 intermediate band the average thickness of bundles. The EHA and wavelet spectra also  
280 highlight the four main period bands, although the 1-m-periodicity is relatively less  
281 relevant. The period bands are not continuous and there are several intervals where the  
282 signal loses power, such as the 11-16 m and 24-36 m intervals of the short period band.  
283 Spectral analysis carried out on MS data corroborate the prevalence of the  
284 abovementioned four period bands, although the intermediate bands do not reach high  
285 confidence levels (Fig. S3).

286 Using the average values of the period bands identified by spectral analysis, the short and  
287 long intermediate period components were separately extracted from the colour data  
288 series through Gaussian bandpass filtering (Fig. 5). The number of oscillations in the short  
289 period filter matches the number of couplets defined in the outcrop and in the colour  
290 curve. Similarly, the oscillations in the intermediate period filter match the number and  
291 thickness of bundles.



292  
 293 Figure 4. Stratigraphic log and chronostratigraphy of the studied section, showing the detrended colour curve. Bundles  
 294 (B) and couplets (C) identified in the sedimentary alternation are numbered in ascending stratigraphic order. The grey  
 295 background shows the extent of the Uptonia jamesoni Black Shale 1, and the pink interval in its upper part shows the  
 296 interval studied herein in detail. The  $2\pi$ -MTM, EHA and Wavelet spectra of the colour data series show the occurrence  
 297 of four main period bands: 30-42 cm (in blue in the  $2\pi$ -MTM spectrum), interpreted as precession (P) couplets; 1 m  
 298 (grey), possibly related to obliquity (O?) cycles; 1.67 m (green), representing short eccentricity (e) bundles; and 5-10  
 299 m (peak at 6.7 m; orange), which corresponds to long eccentricity (E) bundles.



300  
 301 Figure 5. Colour filter outputs of short (in blue) and intermediate (green) period bands, which are related to precession  
 302 couplets and short eccentricity bundles respectively.

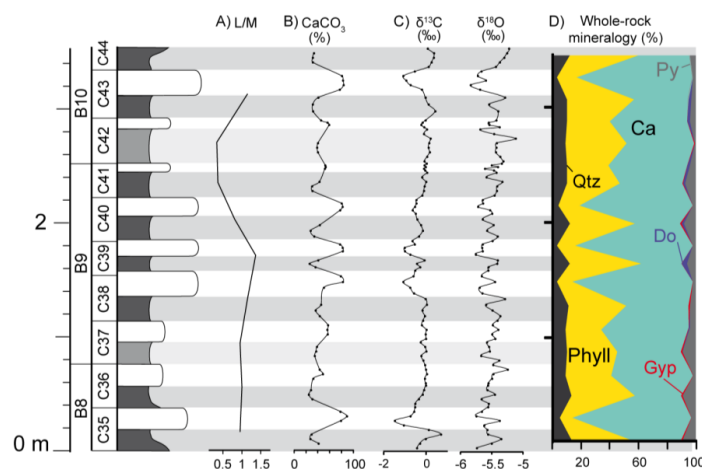
## 303 4.2. Detailed analysis of Bundle 9 (C35-C44 interval)

### 304 4.2.1. L/M ratio and calcium carbonate content



305 The limestone/marlstone (L/M) thickness ratio of couplets varies between 0.33 (C42) and  
306 1.36 (C39), with an average value of 0.90 (Fig. 6A, Table S2). The highest L/M values  
307 are found in the couplets at the central part of bundle B9, while the lowest values  
308 correspond to couplets C41 and C42, at the boundary between bundles B9 and B10.

309 The  $\text{CaCO}_3$  content ranges from 24.63 to 88.97%, averaging out at 49.78% (Fig. 6B;  
310 Table S3). In general, % $\text{CaCO}_3$  fluctuates in line with lithology, limestones and marly  
311 limestones (average: 66.36%) being richer than marls and shales (average: 34.86%).  
312 Marls and shales differ by 10-15% in their  $\text{CaCO}_3$  content, whereas limestone beds at the  
313 central part of bundle B9 show 20-40% more  $\text{CaCO}_3$  than counterpart marly limestones  
314 at bundle boundaries.



315  
316 Figure 6. Lithological log of the Santiurde interval studied in detail (dark grey: shale; pale grey: marl; white: limestone  
317 and marly limestone), showing (A) the limestone–marl (L/M) thickness ratio of couplets, (B) % $\text{CaCO}_3$  content, (C)  
318  $\delta^{13}\text{C}_{\text{carb}}$  and  $\delta^{18}\text{O}_{\text{carb}}$  curves and (D) whole-rock mineralogy. Numbered couplets and bundles are labelled C and B,  
319 respectively. The 0 m level corresponds to 20.34 m of the general section.

#### 320 4.2.2. Carbon and oxygen isotopes

321  $\delta^{13}\text{C}_{\text{carb}}$  values range from -1.5 (C35L) to 0.70‰ (C35M) and average out at -0.25‰ (Fig.  
322 6C). The  $\delta^{13}\text{C}_{\text{carb}}$  curve shows lower values in limy beds and higher values in shales and  
323 marls. The amplitude of the fluctuations is significantly greater in the central couplets of  
324 bundle B9.  $\delta^{18}\text{O}$  values range from -5.84 (C43L) to -5.25‰ (C36L) and average out at -  
325 5.52‰, the  $\delta^{18}\text{O}$  curve being rather spiky.  $\delta^{13}\text{C}_{\text{carb}}$  and  $\delta^{18}\text{O}_{\text{carb}}$  data show intermediate  
326 positive correlation ( $r: 0.53; p < 0.005$ ; Fig. S4A; Table S3).

#### 327 4.2.3. General mineralogy

328 XRD results (Fig. 6D; Table S2) show that calcite is the most abundant mineral in limy  
329 beds and in some of the marl/shales (28 to 84%, average: 54%). Clay minerals constitute  
330 the second most abundant phase (9 to 50%, average: 32%), followed by quartz (3 to 13%,  
331 average: 9%) and other minor components (pyrite, gypsum, and dolomite).

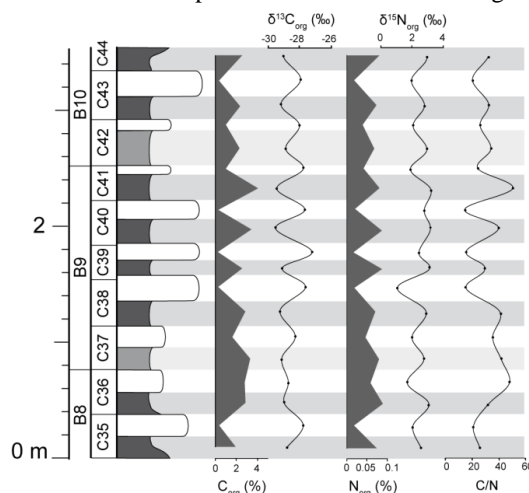


332 The mineralogical content fluctuates in line with lithology, as it shows maximum values  
333 of clays and quartz, and minima of calcite, in marls/shales. Moreover, the amplitude of  
334 the detrital/carbonate mineralogical oscillations increases in the central couplets of bundle  
335 B9. Pyrite, despite being a minor component (0.5 to 9%, average: 4%), also oscillates  
336 with lithology, presenting maximum values in marls/shales, but does not match the  
337 amplitude variation associated with the bundle arrangement.

#### 338 4.2.4. Organic matter geochemistry

339 The content in organic carbon varies between 0.26 (C39L) and 4.03% (C41M) (average  
340 of 1.91%), maximum values being found at black shales. Organic nitrogen also covaries  
341 with lithology, with values ranging from 0.02 (C39L) to 0.09 % (C36M) (average of  
342 0.06%). Both elements show high amplitude oscillations at the central part of bundle B9  
343 and subdued oscillations at bundle boundaries. The relationship between both organic  
344 components was calculated by the C/N ratio (Fig. 7; Table S2)

345  $\delta^{13}\text{C}_{\text{org}}$  values vary between -29.6 (C40M) and -27.2‰ (C40L), and average out at -  
346 28.6‰.  $\delta^{15}\text{N}_{\text{org}}$  ranges from 1.1 (C38L) to 3.2‰ (C40M), with an average value of 2.5‰  
347 (Fig. 7). Both data series alternate in line with lithology, but with opposite trends. The  
348  $\delta^{13}\text{C}_{\text{org}}$  fluctuations at the central couplets of bundle B9 show the greatest amplitude.



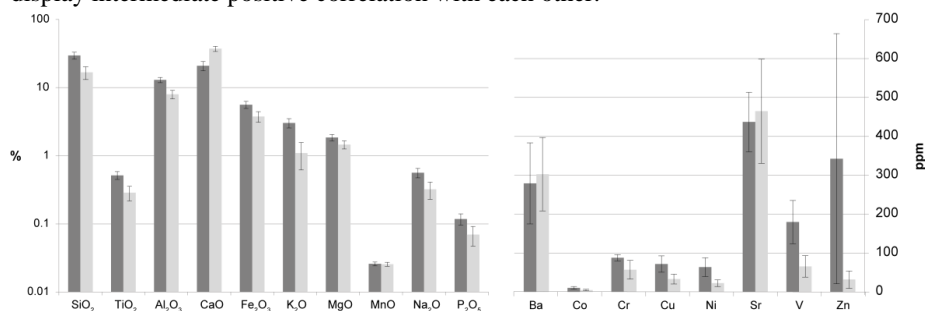
349  
350 Figure 7. Lithological log of the Santiurde interval studied in detail, showing fluctuations in the percentage of organic  
351 C and N, C/N ratio,  $\delta^{13}\text{C}_{\text{org}}$  and  $\delta^{15}\text{N}_{\text{org}}$ .

#### 352 4.2.5. Elemental geochemistry

353 The average abundance of major and trace elements is shown in Fig 8 (Table S4).  $\text{SiO}_2$ ,  
354  $\text{Al}_2\text{O}_3$  and  $\text{CaO}$  constitute 48% of limestones and 63% of marls/shales. Average values  
355 of most major and trace elements are higher in marls and shales than in limy beds, the  
356 exceptions being  $\text{CaO}$ ,  $\text{MnO}$ ,  $\text{Ba}$  and  $\text{Sr}$ . The correlation matrix shows that the abundance  
357 of  $\text{MnO}$  does not correlate with any major and trace elements, but all the other major  
358 elements present strong negative correlation ( $>-0.88$ ) with  $\text{CaO}$  (Table 1) and high  
359 positive correlation with most redox sensitive trace elements ( $\text{Co}$ ,  $\text{Cu}$ ,  $\text{Ni}$ ,  $\text{V}$  and  $\text{Zn}$ ), the



360 only exception being Zn, which shows intermediate positive correlations. Sr and Ba  
 363 display intermediate positive correlation with each other.



362  
 363 Figure 8. The average abundance of major and trace elements of limestones (pale grey) and marl/shales (dark grey).

	SiO <sub>2</sub>	TiO <sub>2</sub>	Al <sub>2</sub> O <sub>3</sub>	CaO	Fe <sub>2</sub> O <sub>3</sub>	K <sub>2</sub> O	MgO	MnO	Na <sub>2</sub> O	P <sub>2</sub> O <sub>5</sub>	Ba	Co	Cr	Cu	Ni	Sr	V	Zn
SiO <sub>2</sub>		9.9E-15	1.2E-09	9.2E-16	5.8E-07	1.3E-11	2.9E-07	0.97	2.3E-06	1.1E-06	6.1E-01	2.6E-07	2.0E-10	2.1E-06	4.3E-05	5.8E-01	2.8E-03	2.3E-02
TiO <sub>2</sub>	<b>0.99</b>		4.0E-10	4.2E-15	4.3E-08	9.4E-14	7.1E-08	0.80	4.8E-06	7.0E-08	5.6E-01	7.5E-07	2.2E-09	8.4E-06	7.9E-05	6.5E-01	8.9E-04	2.0E-02
Al <sub>2</sub> O <sub>3</sub>	<b>0.94</b>	<b>0.95</b>		1.4E-12	6.2E-09	1.3E-12	2.8E-06	1.00	5.4E-07	1.7E-05	9.1E-01	3.2E-04	4.7E-09	5.1E-04	1.1E-03	3.5E-01	1.9E-04	1.4E-02
CaO	<b>-0.99</b>	<b>-0.99</b>	<b>-0.98</b>		1.4E-08	5.3E-15	1.8E-07	0.96	5.7E-07	9.5E-07	6.6E-01	4.7E-06	2.4E-11	9.4E-06	6.2E-05	5.5E-01	4.4E-04	1.7E-02
Fe <sub>2</sub> O <sub>3</sub>	<b>0.88</b>	<b>0.91</b>	<b>0.93</b>	<b>-0.93</b>		6.2E-09	1.8E-06	0.57	7.4E-07	8.1E-06	6.9E-01	1.1E-03	1.1E-06	3.3E-04	6.2E-04	8.2E-01	4.5E-06	1.0E-02
K <sub>2</sub> O	<b>0.97</b>	<b>0.98</b>	<b>0.98</b>	<b>-0.99</b>	<b>0.93</b>		1.8E-06	0.97	1.1E-06	6.1E-07	7.1E-01	1.7E-05	4.5E-09	3.6E-05	1.3E-04	6.9E-01	1.3E-04	1.2E-02
MgO	<b>0.89</b>	<b>0.91</b>	<b>0.86</b>	<b>-0.90</b>	<b>0.86</b>	<b>0.86</b>		0.10	0.00	0.00	0.52	0.00	0.00	0.00	0.00	0.67	0.00	0.14
MnO	-0.01	0.06	0.00	-0.01	0.14	0.01	0.39		0.85	0.62	0.68	0.77	0.75	0.60	0.75	0.82	0.46	0.22
Na <sub>2</sub> O	<b>0.86</b>	<b>0.85</b>	<b>0.88</b>	<b>-0.88</b>	<b>0.88</b>	<b>0.87</b>	<b>0.79</b>	0.05		0.00	0.34	0.01	0.00	0.00	0.00	0.90	0.00	0.02
P <sub>2</sub> O <sub>5</sub>	<b>0.87</b>	<b>0.91</b>	<b>0.82</b>	<b>-0.87</b>	<b>0.84</b>	<b>0.88</b>	<b>0.80</b>	0.12	<b>0.72</b>		0.53	0.00	0.00	0.00	0.00	0.58	0.00	0.01
Ba	-0.13	-0.14	0.03	0.11	-0.10	-0.09	-0.16	-0.10	-0.23	-0.16		0.43	0.55	0.24	0.26	0.00	0.29	0.91
Co	<b>0.89</b>	<b>0.88</b>	<b>0.74</b>	<b>-0.85</b>	<b>0.69</b>	<b>0.82</b>	<b>0.75</b>	-0.07	<b>0.61</b>	<b>0.85</b>	-0.19		7E-05	1E-09	5E-07	7E-01	8E-02	2E-02
Cr	<b>0.96</b>	<b>0.94</b>	<b>0.93</b>	<b>-0.97</b>	<b>0.87</b>	<b>0.93</b>	<b>0.91</b>	0.08	<b>0.88</b>	<b>0.80</b>	-0.15	<b>0.79</b>		0.00	0.00	0.66	0.00	0.10
Cu	<b>0.86</b>	<b>0.84</b>	<b>0.72</b>	<b>-0.83</b>	<b>0.74</b>	<b>0.80</b>	<b>0.71</b>	-0.13	<b>0.69</b>	<b>0.84</b>	-0.28	<b>0.94</b>	<b>0.77</b>		1E-09	1E+00	2E-02	4E-03
Ni	<b>0.80</b>	<b>0.78</b>	<b>0.69</b>	<b>-0.79</b>	<b>0.71</b>	<b>0.77</b>	<b>0.67</b>	-0.08	<b>0.65</b>	<b>0.78</b>	-0.27	<b>0.88</b>	<b>0.75</b>	<b>0.95</b>		0.9	0.0	0.0
Sr	0.14	0.11	0.23	-0.15	0.06	0.10	0.11	0.05	-0.03	0.14	0.65	0.08	0.11	-0.01	-0.04		0.49	0.98
V	<b>0.65</b>	<b>0.70</b>	<b>0.76</b>	<b>-0.73</b>	<b>0.85</b>	<b>0.77</b>	<b>0.65</b>	0.18	<b>0.82</b>	<b>0.65</b>	-0.26	0.42	<b>0.71</b>	<b>0.52</b>	<b>0.62</b>	-0.17		0.02
Zn	<b>0.52</b>	<b>0.53</b>	<b>0.55</b>	<b>-0.54</b>	<b>0.57</b>	<b>0.56</b>	0.35	-0.29	<b>0.52</b>	<b>0.59</b>	-0.03	<b>0.53</b>	0.39	<b>0.62</b>	<b>0.65</b>	0.01	<b>0.52</b>	

364

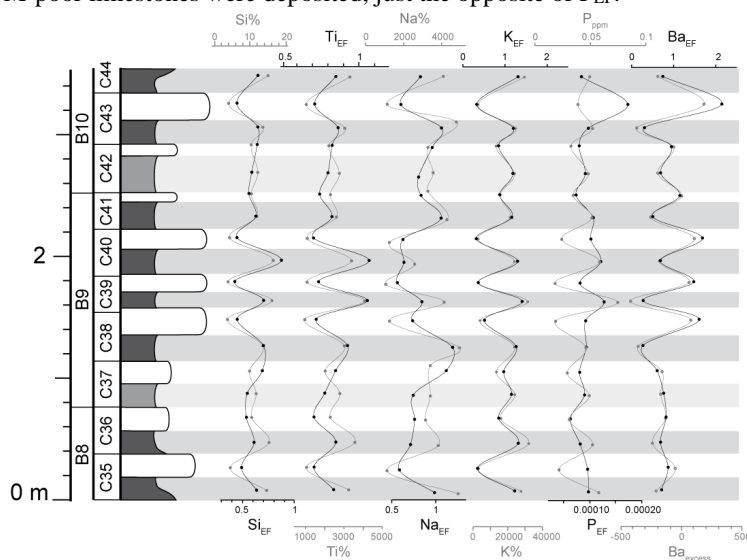
365 Table 1. Pearson correlation coefficient (r) of major and trace element concentrations in the lower left part of the matrix.  
 366 The p-value for each coefficient is located in the upper right part of the matrix. Highest ( $r > \pm 0.65$ ) correlations are  
 367 marked in bold and intermediate correlations ( $r \geq \pm 0.50-0.64$ ) in bold and italics.

368 In order to compare the abundance of some elements with the reference average shale  
 369 composition (Li and Schoonmaker, 2003), enrichment factors ( $X_{EF}$ ; Tribouvillard et al.,  
 370 2006) were calculated as follows:  $X_{EF} = (X/Al)_{sample} / (X/Al)_{average\ shale}$ . Al and K are  
 371 commonly thought to be related to the clay fraction, whereas Si and Ti are often  
 372 associated with the coarser fraction of quartz and heavy minerals (Calvert and Pedersen,  
 373 2007). Enrichment in Ti has also been related to stronger aeolian input (Rachold and  
 374 Brumsack, 2001). In Santiarde  $K_{EF}$ ,  $Ti_{EF}$  and  $Si_{EF}$  covary with lithology, showing  
 375 maximum values in marls/shales and increasing the amplitude of the oscillations in the  
 376 middle part of bundle B9 (Fig. 9).

377 Marine palaeoproductivity is commonly associated with algal growth, which varies with  
 378 the availability of macro-nutrients, such as P and N (Calvert and Pedersen, 2007).  $P_{EF}$   
 379 values from Santiarde show that these deposits are depleted in P (Li and Schoonmaker,  
 380 2003). However,  $P_{EF}$  shows higher values in marls/shales than in limy beds in almost all  
 381 couplets (except in C35L and C43L; Fig. 9). Authigenic Ba in marine sediments is  
 382 commonly associated to barite and its abundance is generally determined by organic C  
 383 export from surface waters into deep marine environments (Tribouvillard et al., 2006). In



384 order to minimize the influence of detrital barium in palaeoenvironmental analyses,  $Ba_{EF}$   
385 and the  $Ba_{excess}$  index are widely used (Dymond et al., 1992).  $Ba_{EF}$  shows that the studied  
386 succession is significantly depleted in Ba in comparison with average shales (Fig. 9, Li  
387 and Schoonmaker, 2003). Both  $Ba_{EF}$  and  $Ba_{excess}$  reveal increased accumulation of Ba  
388 when OM-poor limestones were deposited, just the opposite of  $P_{EF}$ .



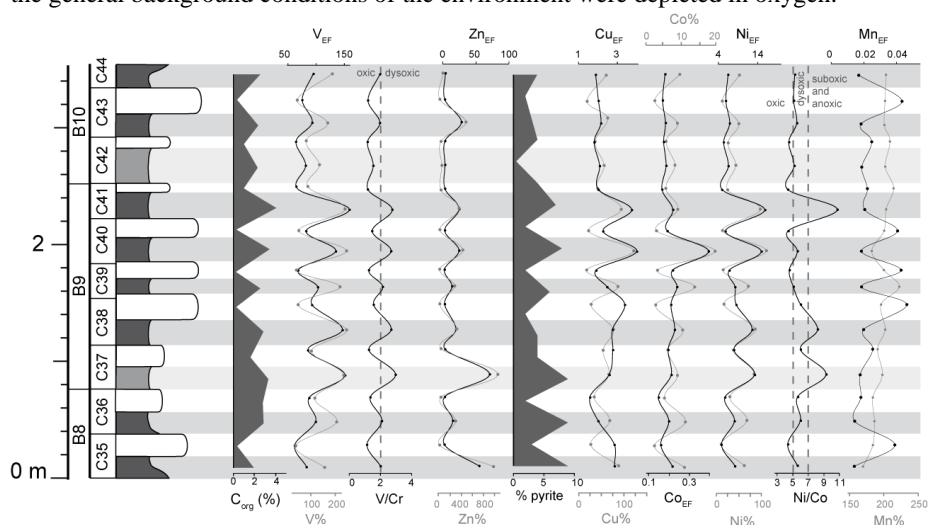
389  
390 Figure 9. Lithological log of the Santiurde interval studied in detail, showing fluctuations in the percentage of elements  
391 related to detrital input (Si, Ti, Na and K), palaeoproductivity (P and Ba) and their enrichment factors (EF). The  $Ba_{excess}$   
392 ratio is also presented.

393  $Mn_{EF}$  is commonly linked to authigenic Mn phases, such as authigenic oxi-hydroxides.  
394 In Santiurde  $Mn_{EF}$  shows an oscillatory pattern in line with lithology, with maximum  
395 values at limestones (Fig. 10). As no evidence of Pliensbachian hydrothermal or volcanic  
396 activity has been reported to date in the area, the higher  $Mn_{EF}$  in limestones could suggest  
397 increased terrestrial input, more oxygenated deep waters or increased remineralization of  
398 organic matter (Bayon et al., 2004; Tribovillard et al., 2006; Calvert and Pedersen, 2007).  
399 Both V and Zn commonly show a strong association with OM content (Calvert and  
400 Pedersen, 2007; Algeo and Liu, 2020). The type of organic matter affects the distribution  
401 of both elements, as V is taken up by tetrapyrrole complexes derived from chlorophyll  
402 decay, whereas Zn is known to be incorporated into humic and fulvic acids (Lewan, 1984,  
403 Aristilde et al., 2012). Enrichment factors of both elements show oscillatory patterns in  
404 line with lithology, with maximum values at shales/marls and a significant enrichment in  
405 V (Fig. 10). On the other hand, Co, Cu and Ni are known to be related with sulphide  
406 fractions (Tribovillard et al., 2006; Algeo and Liu, 2020), as these elements are usually  
407 incorporated as minor constituents in diagenetic pyrite (Berner et al., 2013). With the  
408 exception of  $Cu_{EF}$ , the enrichment factors of these elements also fluctuate with the  
409 lithological alternation, showing maximum values in shales/marls (Fig. 10).

410 Several bielemental ratios associated with redox conditions during sedimentation were  
411 also calculated. According to absolute values of the V/Cr bielemental ratio, most marls



412 and shales deposited under dysoxic conditions, whereas limestones and marly limestones  
413 were accumulated in oxic conditions (Fig. 10; Jones and Manning, 1994). Ni/Co values  
414 from marls and shales support dysoxic or even suboxic/anoxic conditions (Fig. 9, Jones  
415 and Manning, 1994), but suggest that limestones and marly limestones also accumulated  
416 in nearly dysoxic conditions. The discrepancy between V/Cr and Ni/Co results confirms  
417 the limitation of absolute bioelemental ratios to discriminate absolute redox conditions  
418 (Algeo and Liu, 2020). In Santiurde all lithologies are enriched in V, Zn, Ni and Cu when  
419 compared with average shales (Li and Schoonmaker, 2003). The concentration of these  
420 redox-sensitive trace elements is generally higher than in crustal rocks when sediments  
421 accumulate under oxygen depleted conditions (Brumsack, 1986; Arthur et al., 1990).  
422 Consequently, it is assumed that deep seawater oxygen concentration was fluctuating, but  
423 the general background conditions of the environment were depleted in oxygen.

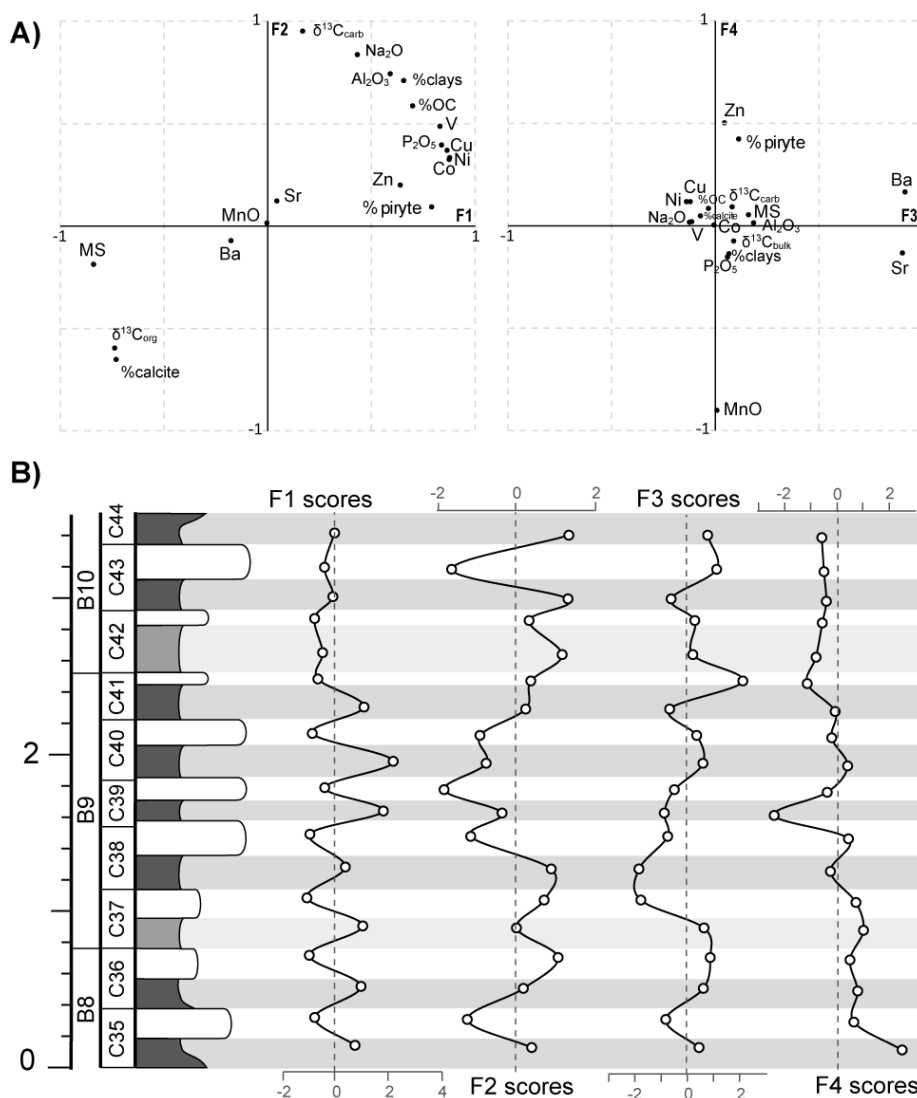


424  
425  
426

Figure 10. Lithological log of the Santiurde interval studied in detail, showing fluctuations in the percentage of redox sensitive elements, their EFs and several bioelemental ratios, along with the organic carbon and pyrite content.

#### 427 4.2.6. Factor analysis

428 A statistical factor analysis was conducted in order to identify key groups of variables  
429 with similar trends in the mineralogical and geochemical databases. As the number of  
430 variables introduced in the analysis has to be lower than the number of cases (samples),  
431 a total of 18 variables of the total dataset were selected. To this end, elements with very  
432 strong mutual correlation coefficients (for example, Mg and Fe with Al) were ignored,  
433 because they would yield redundant data and increase the size of the dataset. Main redox  
434 sensitive elements, in whose Santiurde is enriched, have been included because their  
435 palaeoenvironmental significance. Variables with no quantifiable concentrations  
436 throughout the studied section (e.g., gypsum and dolomite content) were also excluded.  
437 Thus, the analysed dataset consists of 18 variables (see Table S5 and Fig. 11) from 19  
438 cases (beds).



439  
 440 Figure 11. A) Projection of different elements in the Factor 1 versus Factor 2 cross-plot (ca. 70% of the total variance)  
 441 and in the Factor 3 versus Factor 4 cross-plot (ca. 18% of the total variance). B) Stratigraphic distribution of factorial  
 442 scores of the four extracted factors (virtual variables).

443 The optimal factor analysis (varimax rotation) extracted four factors (F1 to F4) or virtual  
 444 variables that have eigenvalues greater than one. These factors explain 87.97% of the  
 445 cumulative variance of the analyzed data matrix (Fig. 11 and Table S5). Factors 1 and 2  
 446 explain the highest percentage of the dataset, 44.54% and 25.78% respectively. Both  
 447 factors explain the variance of variables linked to the lithological alternation and the  
 448 arrangement of couplets in bundles (Fig. 11). F1 shows higher loadings for variables  
 449 linked to oxygenation state (trace elements, pyrite,  $\text{C}_{\text{org}}$  vs  $\delta^{13}\text{C}_{\text{org}}$ , MS) and  
 450 palaeoproductivity ( $\text{P}_2\text{O}_3$ ). Conversely, F2 has higher loadings in variables ( $\text{Na}_2\text{O}$ ,  
 451 clay% vs calcite) linked to the dilution of calcite with terrigenous material;  $\delta^{13}\text{C}_{\text{carb}}$  also





452 shows a very high positive loading with F2. Factors 3 and 4 explain a significantly lower  
453 variance of the total dataset, 9.92 and 7.73% respectively. F3 shows very high positive  
454 loadings for Ba and Sr, whereas F4 shows very high negative loadings for MnO and  
455 intermediate positive loading for Zn and pyrite. The scores of factors 3 and 4 do not align  
456 with the lithological arrangement in couplets and bundles, which suggests that they were  
457 not controlled by orbitally influenced environmental conditions.

## 458 **5. Discussion**

### 459 **5.1. Origin of the inorganic sedimentary fluctuations**

#### 460 **5.1.1. Santiurde rhythmites: primary or diagenetic?**

461 Previous studies have shown that the formation of calcareous rhythmites can be caused by  
462 both primary and diagenetic processes. In some cases, rhythmites have been considered to  
463 be primary, being related to secular variations in the environmental conditions that  
464 controlled sedimentation (e.g., Arthur and Dean, 1991; Hinnov and Park, 1999; Dinarés-  
465 Turell et al., 2018; Martínez-Braceras et al., 2023). In other cases, postdepositional  
466 dissolution/cementation processes have been considered the most important (e.g.,  
467 Hallam, 1986; Reuning et al., 2002; Westphal, 2006; Nohl et al. 2021). When differential  
468 diagenesis affects the primary composition of sediments, part of the carbonate dissolves  
469 from marly beds and migrates to limy beds, precipitating as cements (Westphal, 2006).

470 The Santiurde deposits show some signs of diagenetic overprinting, such as the  
471 occurrence of some secondary cements, calcite overgrowths, early framboidal pyrite and  
472 the growth of pyrite in tests (Fig. 3). In fact, the aragonitic and high-Mg calcite  
473 components of limestones, including their micritic matrix, suffered significant re-  
474 crystallization. However, none of the limestone beds displays a nodular geometry, which  
475 is common in successions affected by intense postdepositional dissolution/cementation  
476 processes (Hallam, 1986; Einsele and Ricken, 1991). Quite the opposite, the  
477 characteristics of the beds are continuous for more than 1 km between the Santiurde  
478 motorway and railway sections. Furthermore, petrographic and SEM observations  
479 suggest that fluid migration from marly to limy beds was overall limited. Thus, skeletal  
480 components of marls/shales (Fig. 2 and 3) do not present features of increased compaction  
481 (Munnecke et al., 2001; Westphal, 2006). This was probably related to an original higher  
482 clay content in marls/shales, which hampered fluid migration between beds and avoided  
483 intense dissolution and recrystallization. In addition, clay minerals show primary textures  
484 (such as deformed, broken plates or isolated flakes wrapping other detrital grains), but do  
485 not show any evidence of intense diagenetic recrystallization. In general, the diagenetic  
486 characteristics observed in the Santiurde rhythmites are typical of processes related to  
487 organic matter decay during burial (Rosales et al., 2001).

488 Interestingly, the lithological arrangement in couplets and bundles observed in the  
489 outcrop, combined with the spectral analysis of colour and MS data series, highlight the  
490 presence of sedimentary cycles with three main periodicities in the succession  
491 (6.6:1.67:0.36). This ratio is comparable to the 405:100:20 ratio produced by the



492 superposition of long eccentricity, short eccentricity and precession cycles (Berger and  
493 Loutre, 1994).

494 The abovementioned characteristics strongly suggest that the formation of the Santiurde  
495 rhythmites was primary and responded to orbitally driven climate change episodes. An  
496 orbital control on sedimentation had previously been deduced in other Pliensbachian  
497 successions from nearby areas, such as the Asturian and Iberian basins (Bádenas et al.,  
498 2012; Val et al., 2017; Sequero et al., 2017).

#### 499 **5.1.1. Preservation of the geochemical signal**

500 Although the formation of the Santiurde rhythmites was a result of orbitally paced  
501 environmental variations, some primary sedimentary characteristics (such as chemical  
502 and mineralogical composition, fossil assemblage, or porosity) could have responded in  
503 different ways to diagenesis. Consequently, the geochemical data of the seven limestone-  
504 marl couplets (C35-C44) studied in detail must be analyzed carefully in order to interpret  
505 which environmental variations controlled sedimentation.

506 Whole-rock inorganic isotopic analyses from diagenetically “closed” systems, such as  
507 hemipelagic carbonates, have been used successfully for the climatic reconstruction of  
508 ancient sedimentary environments (e.g., Jenkyns and Clayton, 1986; Marshall, 1992;  
509 Silva et al., 2011; Martínez-Braceras et al., 2017; Deconinck et al., 2020). However,  
510  $\delta^{13}\text{C}_{\text{carb}}$  and  $\delta^{18}\text{O}_{\text{carb}}$  values tend to get depleted during burial, causing a significant  
511 positive correlation between each other when strong deep burial or meteoric diagenesis  
512 affects the succession (Banner and Hanson, 1990; Marshall, 1992; Swart, 2015). In  
513 Santiurde both isotopic records show depleted values in comparison to Early Jurassic  
514 marine isotopic standard curves (Grossman and Joachimski, 2020; Cramer and Jarvis,  
515 2020). Both  $\delta^{18}\text{O}_{\text{carb}}$  and  $\delta^{13}\text{C}_{\text{carb}}$  records show a positive but not very high correlation  
516 (Fig. S4A;  $r$ : 0.53,  $p < 0.005$ ), following a common burial trend (Banner and Hanson,  
517 1990). This suggests that, although primary isotopic trends may have been preserved,  
518 absolute values are probably distorted. Accordingly,  $\delta^{18}\text{O}_{\text{carb}}$  values from Santiurde are  
519 significantly depleted (Grossman and Joachimski, 2020) and display a spiky curve (Fig.  
520 6). This may reflect the impact of the percolation of diagenetic fluids in post-depositional  
521 processes at low fluid/rock ratios (Banner and Hanson, 1990). Consequently,  $\delta^{18}\text{O}_{\text{carb}}$   
522 values were only used to assess the degree of diagenetic overprinting of other  
523 geochemical proxies.

524 Rosales et al. (2001) analyzed the utility of stable isotopes from Lower-Middle Jurassic  
525 bulk hemipelagic carbonates and fossils (belemnites and brachiopods) from the BCB as  
526 palaeoceanographic proxies. They concluded that whole rock stable isotope records are  
527 not suitable for accurate palaeoceanographic reconstructions because their high OM  
528 content contributed to the alteration of their primary signal. In fact, organic matter  
529 degradation and sulphate reduction in deep sea sediments is known to produce  $\text{CO}_2$   
530 enriched in  $^{12}\text{C}$  and generate early cements with low  $\delta^{13}\text{C}_{\text{carb}}$  (Dickson et al., 2008; Swart,  
531 2015). Accordingly, the generally depleted  $\delta^{13}\text{C}_{\text{carb}}$  values in Santiurde could be a  
532 consequence of the addition of early cements precipitated in equilibrium with isotopically



533 light pore waters affected by OM decay. This process, however, cannot explain the  
534  $\delta^{13}\text{C}_{\text{carb}}$  fluctuations observed along the lithological alternation, because the influence of  
535  $\delta^{13}\text{C}$ -depleted fluids is generally thought to be more pronounced when carbonate content  
536 in the sediment is low and the total organic carbon is comparatively high (Ullman et al.,  
537 2022). Contrarily, in Santiurde maximum  $\delta^{13}\text{C}_{\text{carb}}$  values are recorded in marls/shales and  
538 the crossplot of  $\delta^{13}\text{C}_{\text{carb}}$  versus  $\text{CaCO}_3$  values shows a high negative correlation ( $r$ : -0.75,  
539  $p < 0.005$ ; Fig. S4B). It can therefore be assumed that the high clay content and low  
540 porosity in marls/shales probably hampered a more intense cementation during early  
541 diagenesis (Arthur and Dean, 1991).

542 In line with the above argumentation,  $\delta^{13}\text{C}_{\text{carb}}$  records of hemipelagic carbonates are  
543 commonly used in palaeoclimatic studies because they are not strongly affected by the  
544 bicarbonate composition and temperature of interstitial waters (Marshall, 1992;  
545 Mackensen and Schmiedl, 2019). However, dissolution of aragonite and high-Mg calcite  
546 components, which are generally more abundant in shallow marine areas, and  
547 precipitation of more stable low-Mg calcite phases are important post-depositional  
548 process causing carbon isotope fractionation (Reuning et al., 2002). Aragonite is  
549 generally characterized by more positive  $\delta^{13}\text{C}$  values than high- or low-Mg carbonates  
550 (Swart, 2015). Therefore, a fluctuating rate of aragonitic input could produce covarying  
551  $\delta^{13}\text{C}_{\text{carb}}$  and  $\% \text{CaCO}_3$  records (Reuning et al., 2002), like that found in Santiurde.  
552 However, given that minimum  $\delta^{13}\text{C}_{\text{carb}}$  values are found at  $\% \text{CaCO}_3$  maxima in Santiurde,  
553 it can be concluded that the carbonate distribution does not record variations in the supply  
554 of platform-derived fine-grained aragonitic and high-Mg calcite.

555 Whole rock  $\delta^{13}\text{C}$  and  $\delta^{18}\text{O}$  average values similar to those obtained in Santiurde were also  
556 found in the coeval Rodiles hemipelagic section from the Asturian basin (Deconinck et  
557 al., 2020), that isotopic trend being considered to reveal primary environmental changes.  
558 In fact,  $\delta^{18}\text{O}_{\text{carb}}$  values from Santiurde are within the average range of those obtained from  
559 Pliensbachian belemnites from the Asturian basin (Gómez et al., 2016; Armendáriz et al.,  
560 2012), which were used for palaeoceanographic reconstructions. Taking everything into  
561 account, it can be concluded that the  $\delta^{13}\text{C}_{\text{carb}}$  record from Santiurde may reflect the  
562 original isotopic composition of seawater, but it cannot be excluded that the fluctuations  
563 respond to original variations in the isotopic signal of pore waters. However, the  
564 elemental geochemical evidence further suggests that, in addition to the original  
565 composition and porosity of the different layers, the Santiurde rhythmites also records  
566 variations in the supply of terrigenous components. Thus, diagenetically inert trace  
567 elements, such as  $\text{Ti}_{\text{EF}}$ , also show variations in line with the lithological alternation (Nohl  
568 et al., 2021).

569 Other elements, such as Sr, Fe and Mn, are sensitive to burial and may be used to assess  
570 the degree of diagenetic overprinting in carbonates in combination with  $\delta^{18}\text{O}_{\text{carb}}$  values  
571 (Marshall, 1992; Rosales et al., 2001; Zhao and Zheng, 2014). In general, during  
572 diagenesis, marine carbonates tend to become depleted in Sr and  $\delta^{18}\text{O}$ , but enriched in Fe  
573 and Mn (Banner and Hanson, 1990). There is no correlation between the abundance of  
574 these three elements in Santiurde (Fig. S5; Sr-Mn  $r$ : 0.03,  $p$ : 0.9; Sr-Fe  $r$ : 0.06,  $p$ : 0.82;



575 Mn-Fe r: 0.14, p: 0.58). Moreover,  $\delta^{18}\text{O}_{\text{carb}}$  values do not display any correlation with Sr  
576 and Mn and show positive correlation with Fe, just the opposite of what should be  
577 expected from postdepositional distortion. Similarly, if compared with the average shale  
578 composition (Li and Schoonmaker, 2003), both limestones and marls from Santiurde are  
579 significantly enriched in Sr (402.5 ppm), slightly enriched in Fe (32750 ppm), and  
580 depleted in Mn (199 ppm). Taking everything into account a strong diagenetic  
581 overprinting can be ruled out.

582 In conclusion, burial diagenesis produced depleted inorganic stable isotope values, but  
583 there are no signs of strong differential diagenesis or postdepositional redistribution of  
584 geochemical components in the Santiurde section. The  $\delta^{13}\text{C}_{\text{carb}}$  signal was affected by  
585 early diagenetic processes related to OM decay in limestones, but not to the extent of  
586 obscuring the original fluctuating trend.

## 587 **5.2. Organic matter: fluctuating composition and preservation**

588 Detailed multiproxy analysis carried out throughout 7 limestone-marl couplets from the  
589 oldest BS cast light on the origin of OM and the sedimentary factors that controlled its  
590 distribution. Rosales et al. (2006) showed that BS intervals accumulated during second  
591 order sea level rises, which originated the flooding of large continental areas and the  
592 creation of a moderately isolated epicontinental sea, in which water circulation was  
593 relatively restricted. More specifically, sluggish circulation at the depocentres of the  
594 irregular floor of the BCB contributed to increasing density stratification of the water-  
595 column and caused a sea floor depleted in oxygen (Wignall, 1991; Quesada et al., 2005),  
596 which prevented oxidation of the high organic matter content of the section.

### 597 **5.2.1. Composition of OM**

598 Previous studies demonstrated that the greatest part of the organic matter found in the  
599 BCB Pliensbachian black shales had a marine origin, being dominated by amorphous and  
600 structured liptinitic organic matter (Suárez-Ruiz and Prado, 1987; Quesada et al., 1997,  
601 2005; Permanyer et al., 2013). The study of saturated biomarkers corroborated a dominant  
602 pattern of mature extracts derived from marine algal components. Additionally, SEM  
603 analysis carried out in the present study provided evidence of the occurrence of biofilms  
604 with sporadic occurrences of vitrinite (Fig. 3E and F).

605 The average organic C/N ratio of 30.45 obtained in Santiurde (Fig. 7) is significantly  
606 higher than that of modern marine organic matter, which usually displays values between 5  
607 and 18 (Meyers, 2006). However, C/N ratios observed in current reservoirs cannot be  
608 directly extrapolated to ancient rocks, especially to those deposited under high  
609 productivity conditions (Nijenhuis and Lange, 2000; Meyers et al., 2006; Schneider-Mor  
610 et al., 2012). Meyers et al. (2006) observed that organic components from Albian to  
611 Santonian black shales from Demerara Rise were mainly marine in origin, but their C/N  
612 ratio varied between 20 and 45, which is commonly assigned to terrestrial plants. Those  
613 high C/N values were related to a more rapid recycling of N than C during OM  
614 decomposition. Under oxic to anoxic conditions, modern marine organic matter is



615 commonly degraded via denitrification, decomposing principally nitrogen-rich  
616 aminoacids and reducing the total organic N of sediments (Altabet et al., 1995; Van Mooy  
617 et al., 2002). Thus, high C/N values of some Mediterranean sapropels and Cretaceous  
618 black shales have been related to the drawdown of dissolved oxygen in the water column  
619 under conditions of high export productivity (Nijenhuis and Lange, 2000; Schneider-Mor  
620 et al., 2012). Similar processes might have controlled OM degradation in Santiurde,  
621 producing the abovementioned high C/N ratio. In this regard, considering that the C/N  
622 ratio of typical marine OM is closer to ~6, at least ~23% of the original N must have been  
623 removed from the Santiurde deposits due to denitrification. This percentage is higher than  
624 that calculated by experimentation (~9%) in recent sediments (Van Mooy et al., 2002),  
625 but significantly lower than the 70% deduced from Cretaceous indurate successions  
626 (Schneider-Mor et al., 2012). This suggests that other processes related to OM  
627 degradation, as well as the duration of the process, determine the loss of N due to  
628 differential degradation.

629 The  $\delta^{13}\text{C}_{\text{org}}$  signal from Santiurde is also relatively depleted if compared to modern  
630 marine OM, being closer to values of terrestrial plants (Schneider-Mor et al., 2012).  
631 However, similarly depleted  $\delta^{13}\text{C}_{\text{org}}$  values of marine OM have also been found in other  
632 indurate successions (Nijenhuis and Lange, 2000; Schneider-Mor et al., 2012). This  
633 general depletion of  $\delta^{13}\text{C}_{\text{org}}$  compared to average algal tissue is associated with selective  
634 decomposition of carbohydrates and proteins enriched in  $^{13}\text{C}_{\text{org}}$ , which are more easily  
635 decomposed, and the fortification of the lipid fraction enriched in  $^{12}\text{C}_{\text{org}}$  (Jenkyns and  
636 Clayton, 1986). A similar fractionation process was invoked in other sections, such as the  
637 Cretaceous oil shales from Israel (Schneider-Mor et al., 2012) and the Mediterranean  
638 Pliocene sapropels (Nijenhuis and Lange, 2000).

639 In conclusion, poorly oxygenated background conditions of bottom waters triggered  
640 denitrification of marine OM in Santiurde, promoting a selective decomposition of  
641 nitrogen-rich aminoacids and the fraction enriched in  $^{13}\text{C}_{\text{org}}$ . This process may have been  
642 stronger during the deposition of OM-rich shales.

### 643 **5.2.2. Fluctuations in OM content and characteristics**

644 In Santiurde, the OM content fluctuates in line with lithology, suggesting that the  
645 environmental factors that controlled its accumulation and/or preservation varied  
646 cyclically (Fig. 7). The fluctuations in OM content could be the result of variations in  
647 either the flux of organic matter to the sea floor (i.e., fluctuations in productivity), or the  
648 rate of dilution by terrestrial or carbonate sedimentary inputs, or the rate of organic-matter  
649 remineralization (i.e., fluctuations in preservation) due to changing seawater oxygen  
650 concentrations (Tyson, 2005; Swart et al., 2019).

651 Many factors affect sedimentary  $\delta^{13}\text{C}_{\text{org}}$  values of marine sediments, such as biological  
652 sources, recycling of organic matter, and marine productivity (e.g., Nijenhuis and Lange,  
653 2000; Tyson, 2005; Meyers et al., 2006; Luo et al., 2014). Changes in marine productivity  
654 can be ruled out for the Santiurde  $\delta^{13}\text{C}_{\text{org}}$  fluctuations. Indeed, increased OM production  
655 generally results in greater sequestration of  $^{12}\text{C}$ , which would originate higher  $\delta^{13}\text{C}_{\text{org}}$



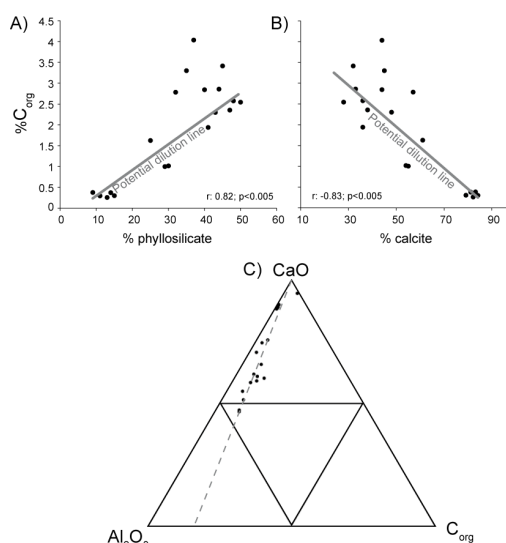
656 values when OM content increased (Meyers et al., 2006), just the opposite of the Santiurde  
657 trend (Fig. 7). This is also confirmed by  $\delta^{15}\text{N}_{\text{org}}$  values, which can also be subject to  
658 fractionation due to variations in productivity. N is assimilated by organisms in order to  
659 produce biomass, preserving the  $\delta^{15}\text{N}_{\text{org}}$  value of its source. Marine  $\delta^{15}\text{N}_{\text{org}}$  values are  
660 influenced by changes in ocean circulation, biological pump, large scale N cycling, and  
661 redox conditions (Robinson et al., 2012). Nitrogen isotopes have been used as a powerful  
662 tool in the analysis of petroleum systems in order to evaluate unconventional reservoirs,  
663 deduce palaeoenvironmental conditions, and assess organic matter sources (Quan and  
664 Adeboye, 2021). However,  $\delta^{15}\text{N}_{\text{org}}$  values may also be subject to distortions during  
665 sedimentation, burial diagenesis, catagenesis and hydrocarbon migration (Robinson et al.,  
666 2012; Quan and Adeboye, 2021). Average  $\delta^{15}\text{N}_{\text{org}}$  values from Santiurde (Fig. 7) are close  
667 to the current ocean isotopic ratio (~5‰; Robinson et al., 2012) and vary within the range  
668 observed in other organic-rich sediments and rocks (principally shales and marlstones;  
669 Holloway and Dahlgren, 2002). Increased N fixation rates have been observed in modern  
670 and ancient marine records in episodes of increased nutrient supply modulated by  
671 precession cycles (Higginson et al., 2003; Swart et al., 2019). In such cases, low  $\delta^{15}\text{N}_{\text{org}}$   
672 values come with increased primary productivity and OM accumulation, just the opposite  
673 of the relationship found in Santiurde. Alternatively, in other marine records, the shallow  
674 water  $\delta^{15}\text{N}_{\text{org}}$  signal suffered fractionation due to the liberation of bottom waters enriched  
675 in  $^{15}\text{N}_{\text{org}}$  (upwelling systems; Altabet et al., 1995). In those cases, marine productivity  
676 increased due the liberation of nutrients stored in the sea bottom and greater OM with  
677 relatively higher  $\delta^{15}\text{N}_{\text{org}}$  signal was produced. However, the restricted palaeogeographic  
678 setting and the sedimentary features preserved (absence of phosphatic and glauconitic  
679 deposits) do not support the influence of upwelling currents in Santiurde.

680 Average  $P_{\text{EF}}$  values from Santiurde are relatively depleted in P (Li and Schoonmaker,  
681 2003), but the  $P_{\text{EF}}$  record displays a fluctuating trend with maxima at OM-rich  
682 marls/shales (Fig. 9). Greater accumulation of P in marls/shales suggests that OM might  
683 have increased due to enhanced marine productivity (Calvert and Pedersen, 2007).  
684 Although Ba related indexes would not support this interpretation, it should be taken into  
685 account that authigenic barite dissolves when bottom water oxygenation is limited  
686 (Dymond et al., 1992; Tribovillard et al., 2006). Consequently, it is possible that the Ba  
687 content does not reflect palaeoproductivity ratios.  $P_{\text{EF}}$  data support a relationship between  
688 greater OM accumulation and higher palaeoproductivity, driven by the intensification of  
689 nutrient input (Tribovillard et al., 2006; Swart et al., 2019). However, a more  
690 comprehensive palaeoecological study should be carried out in order to explore whether  
691 OM fluctuations corresponded to actual variations in palaeoproductivity.

692 Fluctuations in the rate of dilution of OM by non-organic components can also result in  
693 an alternation of organic-rich and organic-poor beds (Bohacs et al., 2005). In Santiurde  
694  $C_{\text{org}}$  and phyllosilicate content show a strong positive correlation ( $r: 0.82$ ;  $p < 0.005$ ; Fig.  
695 12A) and covary in line with the rhythmic succession. This shows that  $C_{\text{org}}$  oscillations  
696 were not caused by variations in the rate of dilution by clays. The  $\text{CaO-Al}_2\text{O}_3\text{-}C_{\text{org}}$  ternary  
697 plot (Fig. 12C) also illustrates that the  $C_{\text{org}}/\text{Al}_2\text{O}_3$  ratio is relatively constant, whereas a



698 higher variability is observed in the  $\text{CaO}/\text{Al}_2\text{O}_3$  and  $C_{\text{org}}/\text{CaO}$  ratios. Therefore,  $C_{\text{org}}$   
699 fluctuations could have resulted from cyclic variations in the dilution rate by calcite input.  
700 In fact, the crossplot between calcite and  $C_{\text{org}}$  shows a strong negative correlation (Fig.  
701 12B;  $r: -0.83; p < 0.005$ ), which is typical of dilution driven OM fluctuations (Arthur and  
702 Dean, 1991; Beckmann et al., 2005). In order to disentangle the origin of the cyclic  
703 sedimentation, bed thickness and duration must be taken into consideration (Einsele and  
704 Ricken, 1991). If variations in the rate of carbonate sedimentation had been the only  
705 process controlling organic matter dilution, while OM and clay mineral inputs stayed  
706 constant, limestone would have been significantly thicker than marls/shales, which is  
707 not the case in Santiurde (Fig. 6A). This suggests that a greater input of clay minerals  
708 must also have occurred during the deposition of marls/shales. Moreover, samples with  
709 higher clay mineral content and lower calcite content display greater dispersion in the  $C_{\text{org}}$   
710 vs calcite crossplot (Fig. 12B). This pattern suggests that when marl/shales were being  
711 deposited, there might have been another factor controlling OM content, such as changes  
712 in OM production or preservation (Bohacs et al., 2005).



713  
714 Figure 12. Crossplot of  $C_{\text{org}}$  against (A) phyllosilicate and (B) calcite content. Potential dilution lines of  $C_{\text{org}}$  are marked  
715 in both graphs. C) Ca-Al- $C_{\text{org}}$  ternary plot with Santiurde samples, which follow a constant  $C_{\text{org}}/\text{Al}_2\text{O}_3$ .

716 Accordingly, the sedimentological and geochemical evidence strongly suggests that the  
717 fluctuations in OM content found in the Santiurde rhythmite were closely related to  
718 variations in the rate of organic-matter remineralization (preservation) as a consequence  
719 of secular variations in seawater oxygen concentrations. Thus, the characteristics of  
720 shales, such as well-preserved lamination, absence of burrows and the scarcity of benthic  
721 fauna (Figs. 2 and 3), strongly suggest that the sea bottom was depleted in oxygen.  
722 Conversely, bioturbation structures and benthic fauna are more diverse and abundant in  
723 limestones, suggesting a better oxygenation of the seabed (Figs. 2 and 3). Changing redox  
724 conditions can also be deduced from  $\delta^{13}\text{C}_{\text{org}}$  records (Algeo and Liu, 2020). Microbial  
725 chemoautotrophy, which is typical of oxygen-depleted environments, fixes carbon



726 enriched in  $^{12}\text{C}$ , producing lower  $\delta^{13}\text{C}_{\text{org}}$  values than OM produced by photosynthetic  
727 eukaryotic algae (Nijenhuis and Lange, 2000; Luo et al., 2014). Accordingly, minima in  
728  $\delta^{13}\text{C}_{\text{org}}$  from OM-rich marls/shales from Santiurde are very likely related to reducing  
729 deep-water conditions, similar to those deduced for some Pliocene Sapropels (Nijenhuis  
730 and Lange, 2000). The strong negative correlation between  $\text{C}_{\text{org}}$  content and  $\delta^{13}\text{C}_{\text{org}}$  ( $r$ : -  
731 0.945,  $p < 0.0001$ ) supports the close relationship between seabed oxygenation conditions  
732 and OM preservation. This interpretation is in line with that derived from the  
733 abovementioned C/N ratio, which also suggests that denitrification intensified during  
734 deposition of marls/shales due to more reducing sea bottom conditions.

735 The interpretations above are also supported by  $\text{N}_{\text{org}}$  and  $\delta^{15}\text{N}_{\text{org}}$  data. Denitrification can  
736 result in  $\delta^{15}\text{N}_{\text{org}}$  isotope fractionation in poorly oxygenated conditions, as denitrification  
737 and anaerobic ammonium oxidation reactions increase  $^{15}\text{N}_{\text{org}}$  in OM (Robinson et al.,  
738 2012). In Santiurde  $\delta^{15}\text{N}_{\text{org}}$  isotopes fluctuate in line with the lithological rhythmites (Fig.  
739 7), showing maxima at marls/shales and hence a significant negative correlation with  
740  $\delta^{13}\text{C}_{\text{org}}$  ( $r$ : -0.70  $p < 0.005$ ) and positive correlations with  $\text{C}_{\text{org}}$  ( $r$ : 0.66,  $p < 0.005$ ) and  $\text{N}_{\text{org}}$   
741 ( $r$ : 0.73,  $p < 0.005$ ) content. This suggests that both isotopic signals were probably  
742 controlled by similar environmental factors. It can therefore be concluded that  $\delta^{15}\text{N}_{\text{org}}$   
743 values increased during the accumulation of marls/shales, when bottom water  
744 oxygenation decreased and denitrification intensified.

745 Pyrite and  $\text{C}_{\text{org}}$  contents also show an intermediate positive correlation in Santiurde ( $r$ :  
746 0.6,  $p < 0.01$ ). Pyrite might be formed during very early diagenesis due to reactions between  
747 Fe and  $\text{H}_2\text{S}$ .  $\text{H}_2\text{S}$  is generally released into porewaters when sulphate-reducing bacteria  
748 use sedimentary organic matter as a reducing agent and energy source (Berner, 2013).  
749 More oxygenated conditions during the deposition of limestones could have inhibited the  
750 formation of pyrite. Conversely, limestones present higher magnetic susceptibility values  
751 than marls/shales, possibly associated with a greater concentration of magnetite (Fig. S2).  
752 Magnetite could be either detrital in origin or related to postdepositional changes in redox  
753 state, as more oxygenated conditions favour the partial replacement of pyrite with iron  
754 oxides, such as magnetite (Lin et al., 2021).

755 Finally, the correlation matrix (Table 1) and the factor analysis (Fig. 11) also show a close  
756 relationship between some redox sensitive elements (Fig. 10; V, Zn, Co, Cu, Ni), pyrite  
757 and  $\text{C}_{\text{org}}$  content (Calvert and Pedersen, 2007; Algeo and Liu, 2020). Enrichment factors  
758 and ratios highlight a relative enrichment in redox sensitive elements throughout the  
759 succession, which supports the general depositional model of a sea floor depleted in  
760 oxygen (Quesada et al., 2005; Rosales et al., 2006). Trace-metal enrichment factors and  
761 elemental ratios associated with both sulphides and organic matter vary in line with the  
762 lithological rhythmites and support the interpretation of alternating environmental redox  
763 conditions. Similarly, a higher content in authigenic Barite in limestones may indicate  
764 more oxygenated conditions.

765 To sum up, the multiproxy analyses shows that the higher  $\text{C}_{\text{org}}$  content in marls/shales  
766 was related to less oxygenated sea-bottom conditions, with evidence of slightly increased





767 palaeoproductivity. Given the close relationship between these processes and the  
768 lithological rhythmites, it can be concluded that there must have been an orbitally driven  
769 environmental factor that triggered fluctuations in bottom waters oxygenation and  
770 palaeoproductivity.

### 771 **5.3. Orbitally modulated environmental changes**

772 Previous studies of North Iberian Pliensbachian records have demonstrated that this area  
773 was subject to semi-arid climatic conditions, physical erosion being prevalent in the  
774 continent and seawater being temperate (Rosales et al., 2004; Armendáriz et al., 2012,  
775 Gómez et al., 2016; Deconinck et al., 2020). The BCB, being located close to the  
776 boundary between the arid and humid climatic belts at approximately 30°N  
777 palaeolatitude, was especially sensitive to orbitally driven climate change episodes, which  
778 were recorded by the outer ramp hemipelagic rhythmites from Santiurde. These rhythmites  
779 are best characterized in the stratigraphic succession by decimetre-scale calcareous  
780 couplets, which represent precession cycles, and metre-scale bundles linked to short  
781 eccentricity cycles. The imprint of long eccentricity cycles cannot be readily identified in  
782 the field, but can be deduced by spectral analysis. The mutiproxy palaeoenvironmental  
783 analysis carried out herein showed that  $C_{org}$  production and preservation varied in line  
784 with precessional cycles and was modulated by short eccentricity cycles. Although  
785 background oxygenation of the depositional area during the BS deposition was depleted  
786 in oxygen, the astronomically driven environmental changes ultimately determined the  
787 occurrence of lower oxygen conditions at the seabed when marls/shales were being  
788 accumulated and higher oxygenation conditions during limestone accumulation.

#### 789 **5.3.1. Formation of precession driven calcareous couplets**

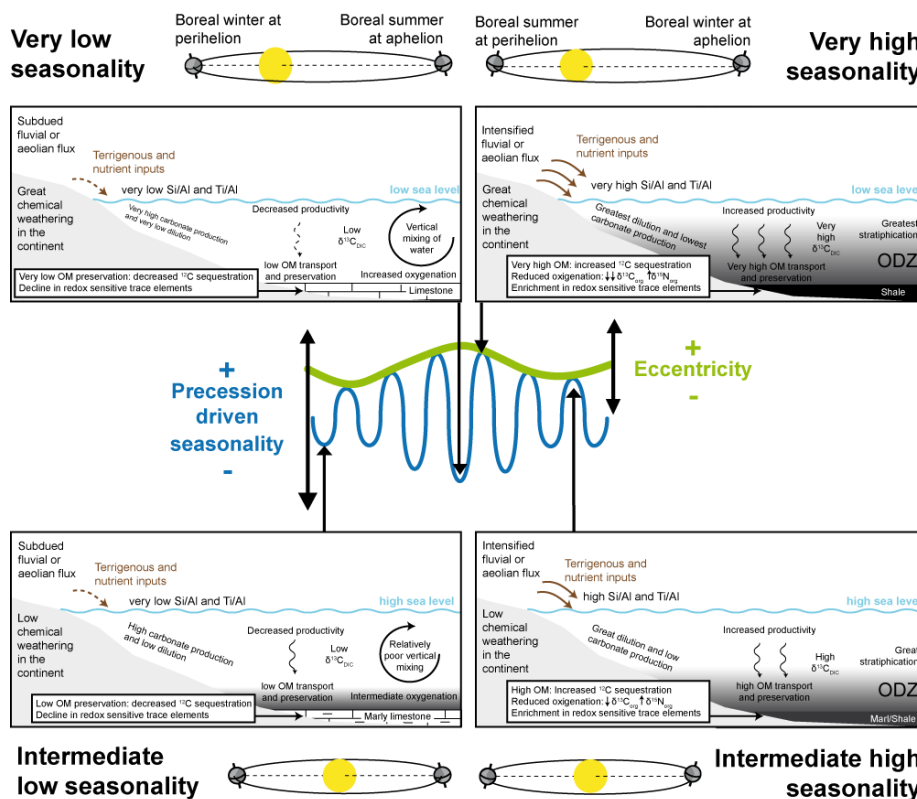
790 The sedimentary processes behind the formation of precession couplets can be analysed  
791 on the basis of thickness relationships between the constituent lithologies (Einsele and  
792 Ricken, 1991). When limy beds are thicker than marly beds, the formation of the  
793 calcareous couplets is commonly attributed to fluctuations in either carbonate dissolution  
794 or carbonate production. Contrarily, marls/shales are usually thicker than limestones  
795 when periodic changes in the rate of dilution of pelagic carbonate by terrigenous  
796 components originate the couplets. Periodic carbonate dissolution can be ruled out in  
797 Santiurde, as there is neither macroscopic nor microscopic evidence of pervasive  
798 carbonate dissolution and the outer carbonate ramp seabed was permanently above the  
799 carbonate compensation depth (Bjerrum et al., 2001). In Santiurde, the low variability of  
800 the  $C_{org}/Al_2O_3$  ratio and the negative relationship between  $CaCO_3$  and  $C_{org}$  indicate that  
801 fluctuations in carbonate input were an important factor in the formation of calcareous  
802 couplets. However, the L/M ratio is close to 1 in most of the couplets (Fig. 6A).  
803 Consequently, the formation of the Santiurde precession driven couplets most likely  
804 responded to periodic changes in both carbonate production and carbonate dilution by  
805 terrigenous material, increasing accumulation and preservation of  $C_{org}$  when marls/shales  
806 deposited. In fact, factor analysis points out that precession driven lithological alternation  
807 (Fig. 11) is strongly associated to redox sensitive variables and terrigenous proxies.



808 Given the generally semiarid Pliensbachian conditions deduced for the BCB (Dera et al.,  
809 2009; Deconinck et al, 2020), a climate characterized by a prolonged dry season and a  
810 short wet season can be envisaged. Dry sub-humid climates, with three to five wet months  
811 per year and a maximum degree of seasonality, produce maximum values of fluvial  
812 sediment discharge into the sea (Cecil and Dulong, 2003). Such high seasonality  
813 conditions are generally produced when the precessional configuration results in summers  
814 occurring at perihelion and winters at aphelion (Fig. 13). In Santiurde both the L/M ratio  
815 and the terrigenous content of couplets suggest that shales/marls were formed in such an  
816 astronomical configuration. Intensified monsoons during the wet season could have  
817 increased the fluvial discharges that reached periplatform areas, producing maxima of  
818 geochemical proxies associated with coarser detrital grain size, such as  $Si_{EF}$  or  $Ti_{EF}$  (Fig.  
819 9; Calvert and Pedersen, 2007). However, inorganic and organic stable isotope records  
820 do not support an increased input of fresh water or terrestrial OM when marls and shales  
821 were being deposited. Alternatively, it is also possible that the terrigenous material was  
822 transported by wind. Indeed, other studies have also related an enrichment in Si and Ti  
823 content in pelagic sediments to stronger aeolian input (Rachold and Brumsack, 2001) and  
824 increased dust production and transportation during high seasonality conditions  
825 (Woodard et al., 2011). Thus, it can be assumed that dust generation increased in the  
826 continents nearby Santiurde during the extremely dry seasons produced at precessional  
827 configurations leading to maximum seasonality. Extreme seasonality conditions may also  
828 have increased dust storms and dust input into the adjacent ocean (McGee et al., 2010).  
829 Either aeolian or fluvial, increased terrigenous input during maximum seasonality  
830 conditions may also have supplied nutrients into the ocean ( $P_{EF}$ ), triggering organic  
831 phytoplackton blooms and organic matter production. This situation promoted greater  
832 OM accumulation and oxygen depletion in deep sea sediments (e.g. Nijenhuis and Lange,  
833 2000; Wang, 2009; Chroustova et al., 2021). Given that the evidence of changing  
834 palaeoproductivity is scarce, it is also possible that orbitally forced mechanisms also  
835 modulated the amount of dissolved oxygen in seawater. As there are no evidences of great  
836 influence of continental water masses that could have promoted density stratification of  
837 the water column (e.g., Arthur and Dean, 1991; Chroustova et al., 2021), it is more likely  
838 that the mechanism was marine in origin. Interestingly, numerical simulations suggested  
839 that during the Late Cretaceous hothouse both precession and eccentricity cycles  
840 modulated seawater ventilation and oxygenation, driven by changes in deep ocean  
841 circulation (Sarr et al., 2022). It is therefore possible that basins that were depleted in  
842 oxygen, like the Santiurde area, were especially sensitive to orbitally forced ventilation  
843 variations. According to the model, the precessional configuration with the higher  
844 seasonality recorded the greatest oxygen depletion at intermediate and deep-water depth,  
845 producing a strong vertical oxygen gradient and seawater stratification. In Santiurde,  
846 similarly reduced vertical mixing may have occurred during the accumulation of  
847 marl/shales, which would have enhanced deep-water anoxia. Indeed, in Early Jurassic  
848 times, lower frequency orbital cycles also triggered periodic changes in the ventilation  
849 and oxygenation of bottom sediments, controlling carbonate and OM accumulation  
850 (Pieńkowski et al. 2021). Thus, the southward flow of Arctic waters from the Boreal Sea  
851 into the Laurasian epicontinental seaway favoured thermohaline circulation and the



852 ventilation of deep waters. However, in periods of high atmospheric CO<sub>2</sub>, more sluggish  
 853 currents or stagnant conditions prevailed due to the influx of warm and saline waters from  
 854 the Tethyan area. It is possible that the early Pliensbachian BCB rhythmites recorded  
 855 similar, but probably weaker, palaeoceanographic changes at precession timescales.  
 856 Anoxic bottom water conditions allowed OM to be preserved, favoured the precipitation  
 857 of authigenic sulphides and the dissolution of Fe and Mn oxo-hydroxides (Capet et al.,  
 858 2013), and altered the organic isotopic signal (enrichment in <sup>13</sup>C<sub>org</sub> and depletion in  
 859 <sup>15</sup>N<sub>org</sub>). Increased OM burial also resulted in a decrease in the <sup>12</sup>C content of inorganic  
 860 carbon dissolved in seawater (Mackensen and Schmiedl, 2019). Although the <sup>13</sup>C<sub>carb</sub>  
 861 signal found in Santiurde records this C storage fractionation, it is not possible to quantify  
 862 the diagenetic imprint.



863 Figure 13. Orbitally tuned depositional model for the formation of the calcareous couplets and bundles from Santiurde.  
 864 Schemes on the left represent environmental conditions during precessional stages with low annual seasonality (boreal  
 865 summertime at aphelion). Schemes on the right represent environmental conditions during precessional stages with  
 866 high annual seasonality stages (boreal summertime at perihelion). The influence of maximum eccentricity is shown at  
 867 the top and that of minimum eccentricity at the bottom. DIC: Dissolved inorganic carbon. ODZ: Oxygen depleted zone.  
 868

869 In contrast, OM-poor limy beds accumulated during low seasonality precessional stages.  
 870 Such low seasonality conditions (mild summers and winters) resulted when summers  
 871 occurred at aphelion and winters at perihelion (Fig. 13). Mild wet and dry seasons caused  
 872 a decrease in detrital input (by wind and rivers), as well as in nutrient supply.  
 873 Consequently, organic matter production and, consequently, bottom water oxygen



874 consumption declined (e.g. Nijenhuis and Lange, 2000; Wang, 2009; Chroustova et al.,  
875 2021). Moreover, according to the orbitally modulated ocean circulation model (Sarr et  
876 al., 2022), low seasonality precessional stages would also have resulted in maximum  
877 values of dissolved oxygen in bottom water. These environmental conditions favoured  
878 vertical mixing of the water column, bringing oxygen to bottom waters, which allowed  
879 the oxidation of organic matter (Capet et al., 2013). Regarding carbonate components,  
880 previous studies have shown that Jurassic shelfal carbonate factories were more efficient  
881 than pelagic ooze in micrite production (Hinnov and Park 1999; Bádenas et al., 2012). It  
882 can therefore be concluded that decreased terrigenous inputs into shallow marine areas  
883 further increased shelfal carbonate mud production, surpluses being exported into deeper  
884 areas (Tucker et al., 2009; Bádenas et al., 2012). Assuming the general  $\delta^{13}\text{C}_{\text{carb}}$  trend to  
885 be primary, the enrichment in  $^{12}\text{C}$  of limestones could correspond to OM balance in the  
886 marine environment (Mackensen and Schmiedl, 2019). Thus, well oxygenated bottom  
887 waters allowed most of the  $^{12}\text{C}$ -rich OM to be oxidized before burial, decreasing the  $\delta^{13}\text{C}$   
888 of inorganic carbon dissolved in seawater.

889 The palaeoenvironmental model derived from the Santiurde precession couplets differs  
890 significantly from those presented by others for lower Pliesbachian successions from NW  
891 and central Europe (Fig. 1; Martinez and Dera, 2015; Hollar et al., 2023). However, it  
892 should be taken into account that these models were developed for successions  
893 accumulated in the humid climatic belt, where wet conditions prevailed throughout the  
894 year and seasonality was generally weak. In such settings, terrigenous and nutrient inputs  
895 increased at precessional configurations with higher seasonality, causing greater  
896 productivity during the wettest season and stronger vertical water mixing during the drier  
897 season. Consequently, the more calcareous OM-poor beds accumulated at high  
898 seasonality precessional stages.

### 899 **5.3.2. Formation of eccentricity driven bundles**

900 During an eccentricity cycle, the amplitude of precession-driven seasonality cycles is  
901 modulated by variations in the shape of the orbit of the Earth around the Sun (Berger and  
902 Loutre, 1994). At maximum eccentricity the orbit of the Earth is elliptical and,  
903 consequently, insolation changes as much as 24% in one single year, causing significantly  
904 contrasting seasonality conditions. In the northern hemisphere seasonality is maximized  
905 when summers occur at perihelion and winters at aphelion, but seasonality is minimized  
906 when winters occur at perihelion and summers at aphelion (Fig. 13). On the contrary, at  
907 minimum eccentricity the orbit of the Earth is almost circular, which results in relatively  
908 small variations in insolation between aphelion and perihelion, regardless of the  
909 precession-driven orientation of the axis of the Earth. In short, two extreme climatic  
910 situations (maximum and minimum seasonality) alternate throughout 20 kyr precession  
911 cycles at maximum eccentricity, whereas climatic conditions remain stable for longer  
912 periods at eccentricity minima.

913 In Santiurde the arrangement of couplets in bundles is the lithological expression of the  
914 modulation of the amplitude of precession-driven seasonality by eccentricity cycles (Fig.



915 2B). In the interval studied in detail, couplets C36-C37 and C41-C42, located at the  
916 boundaries between bundles B8-B9 and B9-B10, show relatively little lithological  
917 contrast (mals/shales alternating with marly limestones), which suggests formation at  
918 eccentricity minima. The rest of couplets are situated in the central parts of bundles and  
919 show a marked lithological contrast (shales alternating with limestones), which suggests  
920 formation in the two extreme situations that occur during precession cycles at maximum  
921 eccentricity. This amplitude modulation is also recorded by several geochemical and  
922 mineralogical proxies, corroborating the impact of eccentricity cycles on the formation  
923 of the rhytmite.

924 The fluctuations in some redox sensitive ( $C_{org}$ ,  $N_{org}$ , trace elements,  $\delta^{13}C_{org}$ ,  $Mn_{EF}$ ) and  
925 productivity (represented by  $P_{EF}$ ) proxies, some of them associated with Factor 1 in the  
926 factorial analysis (Fig. 11), display greater amplitude during eccentricity maxima. This  
927 suggests that intensified precessional seasonality at maximum eccentricity caused an  
928 increase in terrestrial sediment and nutrient input to the sea, which ultimately resulted in  
929 the intensification of OM production and oxygen consumption (e.g. Nijenhuis and Lange,  
930 2000; Wang, 2009; Chroustova et al., 2021). Precession driven variations in oceanic  
931 currents, which controlled vertical oxygen gradient and seawater stratification, also  
932 contributed to promoting bottom water anoxia in this orbital configuration (Sarr et al.,  
933 2022).

934 On the other hand, limy beds show significant variations in  $CaCO_3$  content (Fig. 6), from  
935 minimum values at bundle boundary couplets (e.g., 32.26% in C36L) to maximum values  
936 in the middle part of the bundles (e.g., 88.98% in C35L). Limy beds in the central part of  
937 bundle B9 also show the lowest content in terrigenous material and coarse-grained detrital  
938 components (Figs. 6 and 9). Conversely, marls/shales show a significantly lower variation  
939 in  $CaCO_3$  content throughout eccentricity cycles (from 24.63 to 45.33% at C35M and  
940 C38M, respectively), although marls in the central part of the bundle display maximum  
941 values in terrigenous material and coarse-grained detrital indices. Therefore, eccentricity  
942 cycles also modulated the low seasonality precessional stages, in which carbonate  
943 accumulation was favoured (Hinnov and Park 1999; Bádenas et al., 2012). At extremely  
944 low seasonality conditions at eccentricity maxima, continental inputs were minimal and,  
945 consequently, so was marine OM production. At the same time, oceanic currents  
946 intensified vertical mixing of water, favouring a well oxygenated water column and  
947 carbonate production (Sarr et al., 2022).

948 Moreover, factor 2, which comprises proxies associated with dilution of carbonate by  
949 terrigenous input, show an interesting trend in line with eccentricity bundles. Scores of  
950 factor 2, in addition to fluctuating with the lithological alternation of calcareous couplets,  
951 also display a larger scale trend with minimum values at eccentricity maxima and  
952 maximum values at eccentricity minima. This trend is mainly produced by  $Na_2O$  and  
953  $^{13}C_{carb}$  (Table S5). Indeed,  $Na_{EF}$  also shows a similar trend, with generally lower values  
954 at eccentricity maxima (Fig. 9). This may record increased chemical weathering in the  
955 continent and the release of  $Na_2O$  (Marshall, 1992). This goes against the orbitally  
956 modulated climatic model of Martinez and Dera (2015), who concluded that chemical



957 wathering increases during low seasonality and annually wet climates developed at  
958 eccentricity minima. Data from Santiurde, however, suggest that the climate was drier at  
959 eccentricity minima.

### 960 **5.3.3. Orbitally paced sea level changes?**

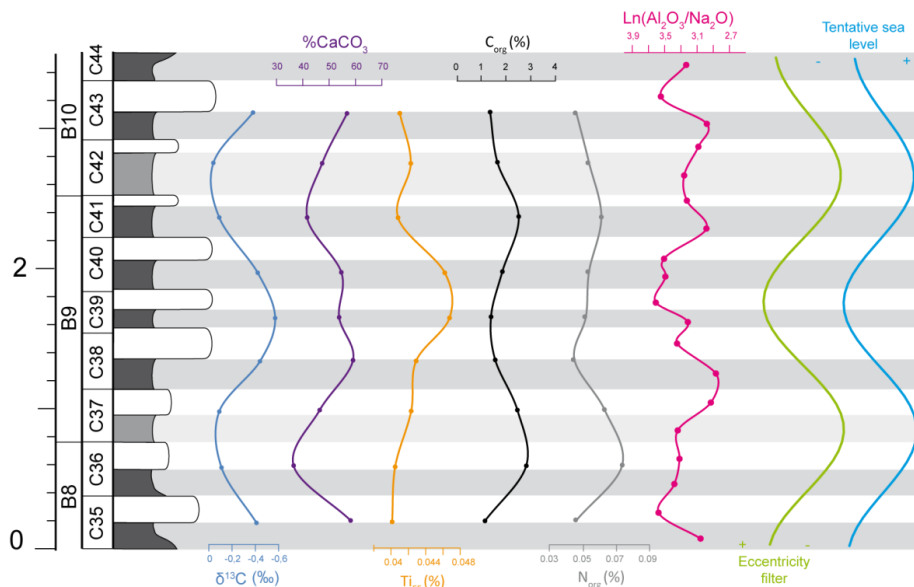
961 It is well known that, during icehouse periods, climate change driven by high-frequency  
962 orbital cycles affects sea level due to fluctuations in the storage of water in continental  
963 ice, causing the so called glacio-eustatic sea level changes (Steffen et al., 2010). High-  
964 frequency sea level changes have also been deduced from many shallow marine platforms  
965 developed in ice-free, greenhouse periods (Haq, 2014). In the absence of extensive ice  
966 caps, sea level changes must have been caused by forcing mechanisms other than  
967 glacioeustasy, which are still debated. The thermal expansion/contraction of water masses  
968 causes sea level changes, but does not produce high amplitude variations (Conrad, 2013).  
969 Fluctuations in water storage in continental areas (principally in aquifers) seems to be a  
970 plausible forcing mechanism of decametric sea level changes during greenhouse  
971 conditions (Wendler and Wendler, 2016). According to the aquifer-eustatic model, low  
972 sea levels occur when large volumes of water are stored in the continents during humid  
973 stages, whereas sea-level rises during dry epochs due to increased aquifer discharge  
974 (Sames et al., 2020). Consequently, in a greenhouse context, orbitally driven alternations  
975 of arid and humid periods can originate 3<sup>rd</sup> and 4<sup>th</sup> order sea level fluctuations (Wendler  
976 and Wendler, 2016; Sames et al., 2020). Greater accumulation of  $\delta^{18}\text{O}$  and  $\delta^{13}\text{C}$  depleted  
977 fresh water in the continent results in heavier  $\delta^{18}\text{O}$  and  $\delta^{13}\text{C}$  of inorganic carbon dissolved  
978 in seawater, and viceversa.

979 Second order sea level changes occurred in Early Jurassic times in the BCB, which were  
980 recorded by  $\delta^{13}\text{C}$  in well preserved belemnites (Rosales et al., 2006). Highstand deposits  
981 show maximum values in OM content and  $\delta^{13}\text{C}$  values in belemnites, while lowstand  
982 intervals are characterized by carbonate-rich sedimentation and lower  $\delta^{13}\text{C}$  values in  
983 belemnites. These carbon-isotope records reflect fluctuations in the  $\delta^{13}\text{C}$  composition of  
984 the inorganic carbon dissolved in seawater, which were controlled by periodic variations  
985 in OM burial and storage of  $^{12}\text{C}$  in the seabed (Quesada et al., 2005; Rosales et al., 2006).  
986 This suggests that water stratification increased and ventilation of the seabed decreased  
987 in highstands. Martinez and Dera (2015) showed that  $\delta^{13}\text{C}$  values from Jurassic and  
988 Lower Cretaceous perythetyan successions also recorded second and third order sea level  
989 changes modulated by orbital cycles. According to this study, flooding of continental  
990 areas at highstands triggered marine productivity and, consequently, seawater  $\delta^{13}\text{C}$  values  
991 increased in neritic domains.

992 In Santiurde, several lines of evidence suggest that short eccentricity cycles could have  
993 modulated sea level. Factor 2 scores (which are greatly influenced by changes in  
994 terrigenous material and  $\delta^{13}\text{C}_{\text{carb}}$ ; see table S5) change in line with eccentricity bundles,  
995 displaying higher values at eccentricity minima and lower values at eccentricity maxima  
996 (Fig. 14). Average  $\delta^{13}\text{C}_{\text{carb}}$ ,  $\% \text{CaCO}_3$  and  $\text{Ti}_{\text{EF}}$  values per couplet show high values at  
997 eccentricity minima. Average  $\text{C}_{\text{org}}$  and  $\text{N}_{\text{org}}$  values per couplet also fluctuate in line with



998 eccentricity bundles, showing maximum (or minimum) values in the intervals that  
999 correspond to low (or high) eccentricity configurations. This may indicate that the average  
1000 OM content per precessional stage was higher at eccentricity minima, although shales at  
1001 eccentricity maxima recorded maximum OM values. Using the abovementioned models,  
1002 it can be postulated that low sea levels may have occurred during eccentricity maxima.  
1003 Lowstand deposits recorded the highest and probably coarsest terrigenous inputs ( $Ti_{EF}$ ;  
1004 Olde et al., 2015), but also the most calcareous sedimentation due to platform  
1005 progradation. A lower sea level would have facilitated seawater ventilation and OM  
1006 degradation at eccentricity scale. However, ventilation at maximum eccentricity  
1007 decreased when precession-driven seasonality increased, which temporarily enhanced  
1008 OM production and preservation, and caused the accumulation of shales on the seabed.  
1009 Similarly, a higher sea level at eccentricity minima could have decreased bottom water  
1010 ventilation, contributing to OM preservation. These conditions promoted OM  
1011 accumulation even if terrigenous and nutrient inputs were not high when shales deposited.



1012  
1013 Figure 14. Lithological log of the Santiurde interval studied in detail, showing the average value per couplet of  $\delta^{13}C_{carb}$ ,  
1014  $\%CaCO_3$ ,  $Ti_{EF}$ ,  $C_{org}$  and  $N_{org}$ . The palaeoweathering index  $Ln(Al_2O_3/Na_2O)$  of all beds, the short eccentricity colour  
1015 filter output (Fig. 5) and a tentative sea level curve are also shown.

1016 Minima of  $N_{aEF}$  at high eccentricity lowstands (Fig. 8) suggest that the climate may have  
1017 been more humid than during low eccentricity highstands. The  $Ln(Al_2O_3/Na_2O)$  index is  
1018 a palaeoweathering index based on a statistical model of linear compositional and  
1019 weathering trends (Von Eynatten et al., 2003). This index is especially recommended for  
1020 rocks with a high percentage of biogenic carbonate (Montero-Serrano et al., 2015), such  
1021 as those from Santiurde.  $Ln(Al_2O_3/Na_2O)$  values in Santiurde show a gradual trend in line  
1022 with eccentricity bundles (Fig. 14). Maximum values, which indicate greater chemical  
1023 weathering in the continent, are recorded at eccentricity maxima. This configuration  
1024 agrees with the aquifer-eustatic sea level model, in which humid climates result in  
1025 increased fresh water storage in the continent and lower sea levels, whereas aquifers are



1026 emptied in drier periods and sea-level rises (Wendler and Wendler, 2016). Jurassic sea  
1027 level changes deduced from shallower areas from the Iberian basin were also associated  
1028 with orbitally paced aquifer-eustatism (Sequero et al., 2017; Val et al., 2017).

#### 1029 **5.3.4. Comparison with orbital forcing during Mesozoic OAEs**

1030 Four Lower Jurassic BS levels occur in the BCB and the Asturian basin (Borrego et al.,  
1031 1996; Rosales et al., 2006). The lower Toarcian BS correlates with the globally recorded  
1032 early Toarcian Oceanic Anoxic Event (T-OAE; Jenkyns and Clayton, 1986; Hesselbo et  
1033 al., 2000; Rosales et al., 2006), which was related to a perturbation in the Earth's climate  
1034 originated by an abrupt addition of  $^{12}\text{C}$  into the carbon cycle. Many studies have  
1035 previously demonstrated the influence of orbital forcing on the T-OAE in western,  
1036 southern and northern Tethys areas (Huang and Hesselbo, 2014; Boulila and Hinnov,  
1037 2017, Boulila et al., 2019). These studies revealed the general prevalence of 405-kyr  
1038 eccentricity cycles in lower Jurassic records, along with a strong expression of both  
1039 precession and obliquity cycles, although the influence of the latter only increased during  
1040 the anoxic event. The palaeoenvironmental changes driven by obliquity cycles produced  
1041 variations in productivity, seabed oxygenation and/or OM origin during the T-OAE (Suan  
1042 et al., 2015). The shift in astronomical forcing during the T-OAE has also been linked  
1043 with the lengthening of the terrestrial productivity season due to increases in global  
1044 temperatures and humidity (Boulila and Hinnov, 2017; Boulila et al., 2019).

1045 In Santiurde, the influence of eccentricity and precession cycles prevailed during the  
1046 formation of the Pliensbachian BS1, with little or no evidence of obliquity forcing.  
1047 Interestingly, however, precession cycles also modulated the palaeoenvironmental  
1048 changes (continental weathering, oceanic productivity and redox conditions) that  
1049 occurred during other Mesozoic OAEs associated with the release of greenhouse gases,  
1050 such as the Cretaceous OAE 1a and 1b events (Giorgioni et al 2015; Benamara et al.,  
1051 2020). It can therefore be concluded that the Pliensbachian BS1 of the BCB shows greater  
1052 similarities with Cretaceous OAEs than with the Toarcian OAE. However, it should be  
1053 noted that most of the astrochronological studies of the Early Jurassic, including those  
1054 focused on orbital forcing on the T-OAE, were previously focused on successions located  
1055 at higher latitudes than Santiurde (Suan et al., 2015; Martinez and Dera, 2015; Boulila  
1056 and Hinnov, 2017; Storm et al., 2020). It is possible that, similar to the eccentricity  
1057 modulated precessional depositional model, climatic belts determined the response of the  
1058 sedimentary environment to similar climatic forcings.

#### 1059 **6. Conclusions**

1060 Lower Pliensbachian organic-rich calcareous rhythmites from the BCB are the expression  
1061 of periodic environmental variations that occurred in the Milankovitch-cycle band. The  
1062 cyclostratigraphic analysis of rock colour and magnetic susceptibility data series showed  
1063 that calcareous couplets represent precession cycles, whereas thicker bundles record short  
1064 eccentricity cycles; the effect of long-eccentricity cycles, despite not being well expressed  
1065 in the field, was also identified.





1066 The integrated sedimentological, mineralogical and geochemical analysis of a short  
1067 eccentricity bundle allowed the identification of the environmental factors that governed  
1068 the formation of the rhythite, as well as the assessment of diagenetic overprinting. Most  
1069 of the compositional parameters record primary characteristics related to the formation of  
1070 the calcareous rhythmites, but inorganic stable isotope records and the distribution of  
1071 several trace elements may have been somewhat affected by diagenesis during burial.  
1072 However, the results allowed the definition of an original orbitally modulated  
1073 depositional model which provides new insight into the formation of lower Pliensbachian  
1074 organic-rich calcareous rhythmites.

1075 The formation of precessional calcareous couplets was regulated by variations in  
1076 carbonate productivity and in dilution by terrigenous supplies. Thus, organic-rich marls  
1077 and shales deposited during precessional configurations which led to marked annual  
1078 seasonality (boreal summer at perihelion and winter at aphelion). Increased seasonal  
1079 rainfall on land and terrigenous input (by rivers or wind) to marine areas boosted organic  
1080 productivity in surface waters. Increased accumulation of organic matter on the seabed  
1081 eventually caused poorly oxygenated bottom waters. Deep-sea desoxygenation and  
1082 seawater stratification were enhanced due to changes in ocean circulation. Conversely,  
1083 limy beds were formed when seasonality was minimal (boreal winter at perihelion and  
1084 summer at aphelion). The consequent decrease in terrigenous inputs favoured a greater  
1085 production and basinward exportation of carbonate sediment in shallow marine areas. A  
1086 lower production of OM and increased vertical seawater mixing due to changes in oceanic  
1087 currents, resulted in the oxidation of organic matter in the deepest environments.

1088 In addition, several proxies support that the precessional contrast between the intensity of  
1089 seasonally controlled environmental factors, such as terrigenous input and oxygenation  
1090 of bottom sea water, diminished when the Earth's orbit was circular (minimum  
1091 eccentricity) and increased when it was more elliptical (maximum eccentricity). The  
1092 available data further suggest that short-term sea level changes may have occurred in line  
1093 with short eccentricity cycles (higher sea level at eccentricity minima), probably through  
1094 orbitally modulated aquifer-eustasy.

1095 The comparison with Lower Jurassic successions from other areas suggests that  
1096 palaeolatitudinal climatic belts played a significant role in the response of the environment  
1097 to astronomically forced climate-change episodes.

## 1098 **7. Competing interests**

1099 The contact author has declared that none of the authors has any competing interests

## 1100 **8. Acknowledgements**

1101 Research funded by projects PID2019-105670GB-I00/AEI/10.13039/501100011033 of  
1102 the Spanish Government (MCIN/AEI) and by the Consolidated Research Group IT602-  
1103 22 of the Basque Government. NM-B is grateful for post-doctoral specialization grants  
1104 DOCREC19/35 and ESPDOC21/49 from the University of the Basque Country



1105 (UPV/EHU) and a Margarita Salas contract (MARSA22/05) of the Spanish Government  
1106 with Next Generation funds from the European Union. Thanks are due to Carl Sheaver  
1107 for his language corrections.

## 1108 9. References

1109 Algeo, T. J. and Liu, J.: A re-assessment of elemental proxies for paleoredox analysis,  
1110 Chem. Geol., 540, 119549, <https://doi.org/10.1016/j.chemgeo.2020.119549>; 2020.

1111 Altabet, M. A., Francois, R., Murray, D. W. and Prell, W. L.: Climate-related variations  
1112 in denitrification in the Arabian Sea from sediment  $^{15}\text{N}/^{14}\text{N}$  ratios, Nature, 373(6514),  
1113 506-509, <https://doi.org/10.1038/373506a0>, 1995.

1114 Aristilde, L., Xu, Y. and Morel, F. M.: Weak organic ligands enhance zinc uptake in  
1115 marine phytoplankton, Environ. Sci. & technol., 46(10), 5438-5445,  
1116 <https://doi.org/10.1021/es300335u>, 2012.

1117 Armendáriz, M., Rosales, I., Bádenas, B., Aurell, M., García-Ramos, J. C. and Piñuela,  
1118 L.: High-resolution chemostratigraphic records from Lower Pliensbachian belemnites:  
1119 Palaeoclimatic perturbations, organic facies and water mass exchange (Asturian basin,  
1120 northern Spain), Palaeogeogr. Palaeoclimatol. Palaeoecol., 333, 178-191,  
1121 <https://doi.org/10.1016/j.palaeo.2012.03.029>, 2012.

1122 Arthur, M. A. and Dean, W. E.: A holistic geochemical approach to cyclomania: examples  
1123 from Cretaceous pelagic limestone sequences, in: Cycles and events in stratigraphy,  
1124 edited by: Einsele, E., Ricken, W. and Seilacher A., Springer -Verlag, New York, 126-  
1125 166, ISBN 0-387-52784-2, 1991.

1126 Aurell, M., Meléndez, G., Olóriz, F., Bádenas, B., Caracuel, J., García-Ramos, J.C., Goy,  
1127 A., Linares, A., Quesada, S., Robles, S., Rodríguez-Tovar, F.J., Rosales, I., Sandoval, J.,  
1128 Suárez de Centi, C., Tavera, J.M., and Valenzuela, M.: Jurassic, in: The Geology of Spain,  
1129 edited by Gibbons, W., and Moreno, M.T, The Geological Society, London, 213-253,  
1130 <https://doi.org/10.1144/GOSPP.11>, 2002.

1131 Bádenas, B., Aurell, M., Armendáriz, M., Rosales, I., García-Ramos, J. C. and Piñuela,  
1132 L.: Sedimentary and chemostratigraphic record of climatic cycles in Lower Pliensbachian  
1133 marl–limestone platform successions of Asturias (North Spain), Sediment. Geol., 281,  
1134 119-138, <https://doi.org/10.1016/j.sedgeo.2012.08.010>, 2012.

1135 Banner, J. L. and Hanson, G. N.: Calculation of simultaneous isotopic and trace element  
1136 variations during water-rock interaction with applications to carbonate diagenesis,  
1137 Geochim. Cosmochim. Acta, 54(11), 3123-3137, [https://doi.org/10.1016/0016-7037\(90\)90128-8](https://doi.org/10.1016/0016-7037(90)90128-8), 1990.

1139 Bayon, G., German, C. R., Burton, K. W., Nesbitt, R. W. and Rogers, N.: Sedimentary  
1140 Fe–Mn oxyhydroxides as paleoceanographic archives and the role of aeolian flux in



- 1141 regulating oceanic dissolved REE, *Earth Planet. Sci. Lett.*, 224(3-4), 477-4,  
1142 <https://doi.org/10.1016/j.epsl.2004.05.033>; 2004.
- 1143 Beckmann, B., Wagner, T. and Hofmann, P.: Linking Coniacian–Santonian (OAE3)  
1144 black-shale deposition to African climate variability: A reference section from the eastern  
1145 tropical Atlantic at orbital time scales (ODP Site 959, off Ivory Coast and Ghana), in:  
1146 *Deposition of Organic-Carbon-Rich Sediments: Models, Mechanisms, and*  
1147 *Consequences*, edited by: Harris, N.B., Society for Sedimentary Geology (SEPM-SSG),  
1148 Special Publication, 82, 125-143, <https://doi.org/10.29/2001PA00073>, 2005
- 1149 Benamara, A., Charbonnier, G., Adatte, T., Spangenberg, J. E. and Föllmi, K. B.:  
1150 Precession-driven monsoonal activity controlled the development of the early Albian  
1151 Paquier oceanic anoxic event (OAE1b): Evidence from the Vocontian Basin, SE France,  
1152 *Palaeogeogr. Palaeoclimatol. Palaeoecol.*, 537, 109406,  
1153 <https://doi.org/10.1016/j.palaeo.2019.109406>, 2020.
- 1154 Berger, A., and Loutre, M.F.: Precession, eccentricity, obliquity, insolation and  
1155 paleoclimates, in: *Long-term Climatic Variations*, NATO ASI Series, edited by Duplessy,  
1156 J.C. and Spyridakis, M.T., Springer, Berlin, 22, 107–151, [https://doi.org/10.1007/978-3-](https://doi.org/10.1007/978-3-642-79066-9_5)  
1157 [642-79066-9\\_5](https://doi.org/10.1007/978-3-642-79066-9_5), 1994.
- 1158 Berner, Z. A., Puchelt, H., Noeltner, T. and Kramar, U. T. Z.: Pyrite geochemistry in the  
1159 Toarcian Posidonia Shale of south-west Germany: Evidence for contrasting trace-element  
1160 patterns of diagenetic and syngenetic pyrites, *Sedimentology*, 60(2), 548-573, doi:  
1161 10.1111/j.1365-3091.2012.01350.x, 2013.
- 1162 Bohacs, K.M., Grabowski, G.J., Carroll, A.R., Mankiewicz, P.J., Miskell, K.J. and  
1163 Schwalbach, J.R.: Production, destruction, and dilution—the many paths to source-rock  
1164 development, in: *Deposition of Organic-Carbon-Rich Sediments: Models, Mechanisms,*  
1165 *and Consequences*, edited by: Harris, N.B., Society for Sedimentary Geology (SEPM-  
1166 SSG), Special Publication, 82, 61-101, <https://doi.org/10.2110/pec.05.82.0061>, 2005.
- 1167 Borrego, A. G., Hagemann, H. W., Blanco, C. G., Valenzuela, M. and De Centi, C. S.:  
1168 The Pliensbachian (Early Jurassic) “anoxic” event in Asturias, northern Spain: Santa  
1169 Mera Member, Rodiles Formation, *Org. Geochem.*, 25(5-7), 295-309,  
1170 [https://doi.org/10.1016/S0146-6380\(96\)00121-0](https://doi.org/10.1016/S0146-6380(96)00121-0), 1996.
- 1171 Boulila, S. and Hinnov, L. A.: A review of tempo and scale of the early Jurassic Toarcian  
1172 OAE: implications for carbon cycle and sea level variations, *Newsl. Stratigr.*, 50(4), 363-  
1173 389, DOI: 10.1127/nos/2017/0374, 2017.
- 1174 Boulila, S., Galbrun, B., Sadki, D., Gardin, S. and Bartolini, A.: Constraints on the  
1175 duration of the early Toarcian T-OAE and evidence for carbon-reservoir change from the  
1176 High Atlas (Morocco), *Glob. Planet. Change.*, 175, 113-128,  
1177 <https://doi.org/10.1016/j.gloplacha.2019.02.005>, 2019.
- 1178 Braga, J.C., Comas-Rengifo, M.J., Goy, A., Rivas, P. and Yébenes, A.: El Lías inferior y  
1179 medio en la zona central de la Cuenca Vasco-Cantábrica (Camino,Santander), in: III



- 1180 Coloquio de Estratigrafía y Paleogeografía del Jurásico de España, Logroño, Spain, 10-  
1181 19 september 1988, Instituto de Estudios Riojanos, Ciencias de la Tierra, Geología, 11,  
1182 17-45, ISBN 84-00-06877-7, 1988.
- 1183 Bougeault, C., Pellenard, P., Deconinck, J. F., Hesselbo, S. P., Dommergues, J. L.,  
1184 Bruneau, L., Cocquerez, T., Laffont, R., Huret, E. and Thibault, N.: Climatic and  
1185 palaeoceanographic changes during the Pliensbachian (Early Jurassic) inferred from clay  
1186 mineralogy and stable isotope (CO) geochemistry (NW Europe), *Glob. Planet. Change.*,  
1187 149, 139-152, <https://doi.org/10.1016/j.gloplacha.2017.01.005>, 2017.
- 1188 Calvert, S.E. and Pedersen, T.F.: Elemental proxies for palaeoclimatic and  
1189 palaeoceanographic variability in marine sediments: interpretations and applications, in:  
1190 Proxies in Late Cenozoic Paleooceanography, edited by: Hillaire-Marcel, C. and De  
1191 Vernal, A., *Developments in Marine Geology Vol. 1*, Elsevier, Oxford, UK, 567–644,  
1192 [https://doi.org/10.1016/S1572-5480\(07\)01019-6](https://doi.org/10.1016/S1572-5480(07)01019-6), 2007.
- 1193 Capet, A., Beckers, J.-M., and Grégoire, M.: Drivers, mechanisms and long-term  
1194 variability of seasonal hypoxia on the Black Sea northwestern shelf – is there any  
1195 recovery after eutrophication?, *Biogeosciences*, 10, 3943–3962,  
1196 <https://doi.org/10.5194/bg-10-3943-2013>, 2013.
- 1197 Cecil, C.B. and Dulong, F.B.: Precipitation models for sediment supply in warm climates.  
1198 In: *Climate Controls on Stratigraphy*, edited by: Cecil C.B. and Edgar N.T., *SEPM Spec.*  
1199 *Publ.*, 77, 21–27, <https://doi.org/10.2110/pec.03.77.0021>, 2003.
- 1200 Charbonnier, G., Boulila, S., Galbrun, B., Laskar, J., Gardin, S. and Rouget, I.: A 20-  
1201 million-year Early Jurassic cyclostratigraphic record and its implications for the chaotic  
1202 inner Solar System and sea-level changes, *Basin Res.*, 1288-1307,  
1203 <https://doi.org/10.1111/bre.12754>, 2023.
- 1204 Chroustová, M., Holcová, K., Laurin, J., Uličný, D., Hradecká, L., Hrnková, M., Čech, S.,  
1205 Hroudá, F. and Jarvis, I.: Response of foraminiferal assemblages to precession-paced  
1206 environmental variation in a mid-latitude seaway: Late Turonian greenhouse of Central  
1207 Europe, *Mar. Micropaleontol.*, 167, 102025,  
1208 <https://doi.org/10.1016/j.marmicro.2021.102025>, 2021.
- 1209 Conrad, C. P.: The solid Earth's influence on sea level. *Geol. Soc. Am. Bull.*, 125(7-8),  
1210 1027-1052, <https://doi.org/10.1130/B30764.1>, 2013.
- 1211 Cramer, B. D. and Jarvis, I.: Carbon isotope stratigraphy, In: *Geologic time scale 2020*,  
1212 edited by: Gradstein, F.M., Ogg, J., Schmitz, M. and Ogg, G.M, Elsevier, Oxford, UK,  
1213 309-343, <https://doi.org/10.1016/B978-0-12-824360-2.00011-5>, 2020
- 1214 Deconinck, J. F., Gómez, J. J., Baudin, F., Biscay, H., Bruneau, L., Cocquerez, T.,  
1215 Mathieu, O., Pellenard, P. and Santoni, A. L.: Diagenetic and environmental control of  
1216 the clay mineralogy, organic matter and stable isotopes (C, O) of Jurassic (Pliensbachian-



- 1217 lowermost Toarcian) sediments of the Rodiles section (Asturian Basin, Northern Spain),  
1218 *Mar. Pet. Geol.*, 115, 104286, <https://doi.org/10.1016/j.marpetgeo.2020.104286>, 2020.
- 1219 Dera, G., Pellenard, P., Neige, P., Deconinck, J.-F., Pucéat, E. and Dommergues, J.-L.:  
1220 Distribution of clay minerals in Early Jurassic Peritethyan seas: palaeoclimatic  
1221 significance inferred from multiproxy comparisons, *Palaeogeogr. Palaeoclimatol.*  
1222 *Palaeoecol.*, 271, 39–51, <https://doi.org/10.1016/j.palaeo.2008.09.010>, 2009.
- 1223 Dickson, J.A.D., Wood, R.A., Al Rougha, H.B. and Shebl, H.: Sulphate reduction  
1224 associated with hardgrounds: Lithification afterburn!, *Sed. Geol.*, 205, 34–39,  
1225 <https://doi.org/10.1016/j.sedgeo.2008.01.005>, 2008.
- 1226 Dinarès-Turell, J., Martínez-Braceras, N. and Payros, A.: High-Resolution Integrated  
1227 Cyclostratigraphy From the Oyambre Section (Cantabria, N Iberian Peninsula):  
1228 Constraints for Orbital Tuning and Correlation of Middle Eocene Atlantic Deep-Sea  
1229 Records, *Geochem. Geophys.*, 19(3), 787-806, <https://doi.org/10.1002/2017GC007367>,  
1230 2018.
- 1231 Dymond, J., Suess, E. and Lyle, M.: Barium in deep-sea sediment: A geochemical proxy  
1232 for paleoproductivity, *Paleoceanography*, 7(2), 163-181,  
1233 <https://doi.org/10.1029/92PA00181>, 1992.
- 1234 Einsele, G. and Ricken, W.: Limestone-marl alternation-an overview. Cycles and events  
1235 in stratigraphy, in: *Cycles and events in stratigraphy*, edited by: Einsele, E., Ricken, W.  
1236 and Seilacher A., Springer -Verlag, New York, 23-47, ISBN 0-387-52784-2, 1991.
- 1237 Giorgioni, M., Keller, C. E., Weissert, H., Hochuli, P. A. and Bernasconi, S. M.: Black  
1238 shales—from coolhouse to greenhouse (early Aptian), *Cretac. Res.*, 56, 716-731,  
1239 <https://doi.org/10.1016/j.cretres.2014.12.003>, 2015.
- 1240 Gómez, J. J., Comas-Rengifo, M. J., and Goy, A.: Palaeoclimatic oscillations in the  
1241 Pliensbachian (Early Jurassic) of the Asturian Basin (Northern Spain), *Clim. Past*, 12,  
1242 1199–1214, <https://doi.org/10.5194/cp-12-1199-2016>, 2016.
- 1243 Grossman, E. L. and Joachimski, M. M.: Oxygen isotope stratigraphy, in: *Geologic Time*  
1244 *Scale 2020*, edited by: Gradstein, F.M., Ogg, J., Schmitz, M. and Ogg, G.M, Elsevier,  
1245 Oxford, UK, 279-307, <https://doi.org/10.1016/B978-0-12-824360-2.00010-3>, 2020.
- 1246 Hallam, A.: Origin of minor limestone-shale cycles – climatically induced or diagenetic,  
1247 *Geology*, 14, 609–612, <https://doi.org/10.1130/0091-7613>, 1986.
- 1248 Haq, B. U.: Cretaceous eustasy revisited, *Global and Planet. change*, 113,  
1249 <https://doi.org/10.1016/j.gloplacha.2013.12.007>, 44-58.
- 1250 Higginson, M. J., Maxwell, J. R. and Altabet, M. A.: Nitrogen isotope and chlorin  
1251 paleoproductivity records from the Northern South China Sea: remote vs. local forcing of  
1252 millennial-and orbital-scale variability, *Mar. Geol.*, 201(1-3), 223-250,  
1253 [https://doi.org/10.1016/S0025-3227\(03\)00218-4](https://doi.org/10.1016/S0025-3227(03)00218-4), 2003.



- 1254 Hinnov, L.A.: Cyclostratigraphy and its revolutionizing applications in the earth and  
1255 planetary sciences, *Geol. Soc. Am. Bull.*, 125(11-12), 1703–1734,  
1256 <https://doi.org/10.1130/B30934.1>, 2013.
- 1257 Hinnov, L.A. and Park, J.J.: Strategies for assessing Early-Middle (Pliensbachian-  
1258 Aalenian) Jurassic cyclochronologies, *Philos. Trans. R. Soc. Lond. A.*, 357,1831–1859.  
1259 <https://doi.org/10.1098/rsta.1999.0403>, 1999.
- 1260 Hollaar, T. P., Hesselbo, S. P., Deconinck, J.-F., Damaschke, M., Ullmann, C. V., Jiang,  
1261 M., and Belcher, C. M.: Environmental changes during the onset of the Late  
1262 Pliensbachian Event (Early Jurassic) in the Cardigan Bay Basin, Wales, *Clim. Past*, 19,  
1263 979–997, <https://doi.org/10.5194/cp-19-979-2023>, 2023.
- 1264 Holloway, J. M. and Dahlgren, R. A.: Nitrogen in rock: occurrences and biogeochemical  
1265 implications, *Global biogeochem. cycles*, 16(4), 65-1,  
1266 <https://doi.org/10.1029/2002GB001862>, 2002.
- 1267 Huang, C. and Hesselbo, S. P.: Pacing of the Toarcian Oceanic Anoxic Event (Early  
1268 Jurassic) from astronomical correlation of marine sections, *Gondwana Res.*, 25(4), 1348-  
1269 1356, <https://doi.org/10.1016/j.gr.2013.06.023>, 2014.
- 1270 Hüsing, S. K., Beniest, A., van der Boon, A., Abels, H. A., Deenen, M. H. L., Ruhl, M.  
1271 and Krijgsman, W.: Astronomically-calibrated magnetostratigraphy of the Lower  
1272 Jurassic marine successions at St. Audrie's Bay and East Quantoxhead (Hettangian–  
1273 Sinemurian; Somerset, UK), *Palaeogeogr. Palaeoclimatol. Palaeoecol.*, 403, 43-56,  
1274 <https://doi.org/10.1016/j.palaeo.2014.03.022>, 2014.
- 1275 Ikeda, M., Bôle, M. and Baumgartner, P. O.: Orbital-scale changes in redox condition and  
1276 biogenic silica/detrital fluxes of the Middle Jurassic Radiolarite in Tethys (Sogno,  
1277 Lombardy, N-Italy): Possible link with glaciation?, *Palaeogeogr. Palaeoclimatol.*  
1278 *Palaeoecol.*, 457, 247-257, <https://doi.org/10.1016/j.palaeo.2016.06.009>, 2016.
- 1279 Jenkyns, H. C. and Clayton, C. J.: Black shales and carbon isotopes in pelagic sediments  
1280 from the Tethyan Lower Jurassic, *Sedimentology*, 33(1), 87-106,  
1281 <https://doi.org/10.1111/j.1365-3091.1986.tb00746.x>, 1986.
- 1282 Jones, B. and Manning, D. A.: Comparison of geochemical indices used for the  
1283 interpretation of palaeoredox conditions in ancient mudstones, *Chem. Geol.*, 111(1-4),  
1284 111-129, [https://doi.org/10.1016/0009-2541\(94\)90085-X](https://doi.org/10.1016/0009-2541(94)90085-X), 1994.
- 1285 Lewan, M. D.: Factors controlling the proportionality of vanadium to nickel in crude oils,  
1286 *Geochim. Cosmochim. Acta*, 48(11), 2231-2238, [https://doi.org/10.1016/0016-7037\(84\)90219-9](https://doi.org/10.1016/0016-7037(84)90219-9), 1984.
- 1288 Li, M., Hinnov, L. and Kump, L.: Acycle: Time-series analysis software for paleoclimate  
1289 research and education, *Comput. and Geosci.*, 127, 12-22,  
1290 <https://doi.org/10.1016/j.cageo.2019.02.011>, 2019.



- 1291 Li, Y. H. and Schoonmaker, J. E.: Chemical composition and mineralogy of marine  
1292 sediments, in: *Treatise on Geochemistry*, edited by: Holland, H.D. and Turekian, K.K.,  
1293 Elsevier, Oxford, UK, 1-35, ISBN: 0-08-044342-7, 2003.
- 1294 Lin, Z., Sun, X., Roberts, A.P., Strauss, H., Lu, Y., Yang, X., Gong, J., Li, G., Brunner,  
1295 B. and Peckmann, J.: A novel authigenic magnetite source for sedimentary magnetization,  
1296 *Geology*, 49 (4), 360–365, <https://doi.org/10.1130/G48069.1>, 2021.
- 1297 Luo, G., Algeo, T.J., Huang, J., Zhou, W., Wang, Y., Yang, H., Richoz, S. and Xie, S.:  
1298 Vertical  $\delta^{13}\text{C}_{\text{org}}$  gradients record changes in planktonic microbial community composition  
1299 during the end-Permian mass extinction, *Palaeogeogr. Palaeoclimatol. Palaeoecol.*, 396,  
1300 119-131, <http://dx.doi.org/10.1016/j.palaeo.2014.01.006>, 2014.
- 1301 Mackensen, A. and Schmiedl, G.: Stable carbon isotopes in paleoceanography:  
1302 atmosphere, oceans, and sediments, *Earth Sci. Rev.*, 197, 102893,  
1303 <https://doi.org/10.1016/j.earscirev.2019.102893>, 2019.
- 1304 Mann, M. E. and Lees, J. M.: Robust estimation of background noise and signal detection  
1305 in climatic time series, *Climatic change*, 33(3), 409-445,  
1306 <https://doi.org/10.1007/BF00142586>, 1996.
- 1307 Marshall, J.: Climatic and oceanographic isotopic signals from the carbonate rock record  
1308 and their preservation, *Geol. Mag.*, 129, 143–160,  
1309 <https://doi.org/10.1017/S0016756800008244>, 1992.
- 1310 Martinez, M. and Dera, G.: Orbital pacing of carbon fluxes by a ~9-My eccentricity cycle  
1311 during the Mesozoic, *P. Natl. Acad. Sci. USA*, 112, 12604–12609,  
1312 <https://doi.org/10.1073/pnas.1419946112>, 2015.
- 1313 Martínez-Braceras, N., Franceschetti, G., Payros, A., Monechi, S. and Dinarès Turell, J.:  
1314 High-resolution cyclochronology of the lowermost Ypresian Arnakatxa section (Basque-  
1315 Cantabrian Basin, western Pyrenees), *Newsl. Stratigr.*, 54, 53-74, DOI:  
1316 10.1127/nos/2022/0706, 2023.
- 1317 Martínez-Braceras, N., Payros, A., Miniati, F., Arostegi, J. and Franceschetti,  
1318 G.: Contrasting environmental effects of astronomically driven climate change on three  
1319 Eocene hemipelagic successions from the Basque–Cantabrian Basin, *Sedimentology*,  
1320 64(4), <https://doi.org/10.1111/sed.12334>; 960-986, 2017
- 1321 McGee, D., Broecker, W. S. and Winckler, G.: Gustiness: The driver of glacial dustiness?,  
1322 *Quat. Sci. Rev.*, 29, 2340–2350, doi:10.1016/j.quascirev.2010.06.009, 2010.
- 1323 Meyers, P. A.: Paleoceanographic and paleoclimatic similarities between Mediterranean  
1324 sapropels and Cretaceous black shales, *Palaeogeogr. Palaeoclimatol. Palaeoecol.*, 235(1-  
1325 3), 305-320, <https://doi.org/10.1016/j.palaeo.2005.10.025>, 2006.
- 1326 Meyers, S. R.: Astrochron: An R Package for Astrochronology, available at:  
1327 <https://CRAN.R-project.org/package=astrochron>, 2014.



- 1328 Meyers, S.R., Sageman, B.B. and Hinnov, L.A.: Integrated quantitative stratigraphy of  
1329 the Cenomanian–Turonian bridge Creek Limestone member using evolutive harmonic  
1330 analysis and stratigraphic modelling, *J. Sediment. Res.*, 71, 628–644,  
1331 <https://doi.org/10.1306/012401710628>, 2001.
- 1332
- 1333 Nijenhuis, I. A. and de Lange, G. J.: Geochemical constraints on Pliocene sapropel  
1334 formation in the eastern Mediterranean, *Mar. Geol.*, 163, 41–63,  
1335 [https://doi.org/10.1016/S0025-3227\(99\)00093-6](https://doi.org/10.1016/S0025-3227(99)00093-6); 2000.
- 1336
- 1337 Nohl, T., Steinbauer, M. J., Sinnesael, M. and Jarochovska, E.: Detecting initial aragonite  
1338 and calcite variations in limestone–marl alternations, *Sedimentology*, 68(7), 3102–3115,  
1339 <https://doi.org/10.1111/sed.12885>; 2021.
- 1340 Olde, K., Jarvis, I., Uličný, D., Pearce, M.A., Trabucho-Alexandre, J., Čech, S., Gröcke,  
1341 D.R., Laurin, J., Švábenická, L. and Tocher, B.A.: Geochemical and palynological sea-  
1342 level proxies in hemipelagic sediments: a critical assessment from the Upper Cretaceous  
1343 of the Czech Republic, *Palaeogeogr. Palaeoclimatol. Palaeoecol.*, 435, 222–243,  
1344 <https://doi.org/10.1016/j.palaeo.2015.06.018>, 2015.
- 1345
- 1346 Osete, M. L., Gómez, J. J., Pavón-Carrasco, F. J., Villalaín, J. J., Palencia-Ortas, A., Ruiz-  
1347 Martínez, V. C., Heller, F.: The evolution of Iberia during the Jurassic from  
1348 palaeomagnetic data, *Tectonophysics*, 502(1–2), 105–120, 2011.
- 1349
- 1350 Pettijohn, F. J. (Ed.): *Sedimentary Rocks* (2nd ed.), Harper and Brothers, New York, 718  
1351 pp., ISBN 10:0060451904, 1957.
- 1352
- 1353 Pieńkowski, G., Schudack, M.E., Bosák, P., Enay, R., Feldman-Olszewska, A., Golonka,  
1354 J., Gutowski, J., Hengreen, G.F.W., Jordan, P., Krobicki, M., Lathuiliere, B., Leinfelder,  
1355 R.R., Michalík, J., M`onnig, E., Noe-Nygaard, N., P`alfy, J., Pint, A., Rasser, M.W.,  
1356 Reisdorf, A.G., Schmid, D.U., Schweigert, G., Surlyk, F., Wetzel, A. and Wong, T.E.:  
1357 Jurassic, in: *The Geology of Central Europe Volume 2: Mesozoic and Cenozoic*, edited  
1358 by McCann, T., Geological Society of London, London, 823–922,  
1359 <https://doi.org/10.1144/CEV2P.2>, 2008.
- 1360 Pieńkowski, G., Uchman, A., Ninard, K., and Hesselbo, S. P.: Ichnology, sedimentology,  
1361 and orbital cycles in the hemipelagic Early Jurassic Laurasian Seaway (Pliensbachian,  
1362 Cardigan Bay Basin, UK), *Global Planet. Change*, 207, 103648,  
1363 <https://doi.org/10.1016/j.gloplacha.2021.103648>, 2021
- 1364 Quan, T. M. and Adeboye, O. O.: Interpretation of nitrogen isotope profiles in petroleum  
1365 systems: a review. *Frontiers in Earth Science*, 9, 705691,  
1366 <https://doi.org/10.3389/feart.2021.705691>, 2021.
- 1367 Quesada, S. and Robles, S.: Características y origen del petróleo de Hontomín, Cuenca  
1368 Vasocantábrica (Norte de España), *Geogaceta*, 52, 169–172, ISSN 2173-6545, 2012.
- 1369 Quesada, S., Dorronsoro, C. Robles, S., Chaler, R. and Grimalt, J.O.: Geochemical  
1370 correlation of oil from the Ayoluengo field to Liassic “black shale” units in the





- 1371 southwestern Basque-Cantabrian Basin (northern Spain), *Org. Geochem.*, 27, 25-40,  
1372 [https://doi.org/10.1016/S0146-6380\(97\)00045-4](https://doi.org/10.1016/S0146-6380(97)00045-4), 1997.
- 1373 Quesada, S., Robles, S. and Rosales, I.: Depositional architecture and transgressive-  
1374 regressive cycles within Liassic backstepping carbonate ramps in the Basque-Cantabrian  
1375 Basin, northern Spain, *J. Geol. Soc.*, 162, 531-548, [https://doi.org/10.1144/0016-764903-](https://doi.org/10.1144/0016-764903-041)  
1376 041, 2005.
- 1377 Rachold, V. and Brumsack, H. J.: Inorganic geochemistry of Albian sediments from the  
1378 Lower Saxony Basin NW Germany: palaeoenvironmental constraints and orbital cycles,  
1379 *Palaeogeogr. Palaeoclimatol. Palaeoecol.*, 174(1-3), 121-14,  
1380 [https://doi.org/10.1016/S0031-0182\(01\)00290-5](https://doi.org/10.1016/S0031-0182(01)00290-5), 2001.
- 1381 Reuning, L., Reijmer, J. J. and Betzler, C.: Sedimentation cycles and their diagenesis on  
1382 the slope of a Miocene carbonate ramp (Bahamas, ODP Leg 166), *Mar. Geol.*, 185(1-2),  
1383 121-142, [https://doi.org/10.1016/S0025-3227\(01\)00293-6](https://doi.org/10.1016/S0025-3227(01)00293-6), 2002.
- 1384 Robinson, R.S., Kienast, M., Luiza Albuquerque, A., Altabet, M., Contreras, S., De Pol  
1385 Holz, R., Dubois, N., Francois, R., Galbraith, E., Hsu, T.-C., Ivanochko, T., Jaccard, S.,  
1386 Kao, S.-J., Kiefer, T., Kienast, S., Lehmann, M., Martinez, P., McCarthy, M., M'obius,  
1387 J., Pedersen, T., Quan, T.M., Ryabenko, E., Schmittner, A., Schneider, R., Schneider-  
1388 Mor, A., Shigemitsu, M., Sinclair, D., Somes, C., Studer, A., Thunell, R. and Yang, J.-  
1389 Y.: A review of nitrogen isotopic alteration in marine sediments, *Paleoceanography*,  
1390 27(4), PA4203, doi:10.1029/2012PA002321, 2012.
- 1391 Rosales, I., Quesada, S. and Robles, S.: Primary and diagenetic isotopic signals in fossils  
1392 and hemipelagic carbonates: the Lower Jurassic of northern Spain, *Sedimentology*, 48(5),  
1393 1149-1169, <https://doi.org/10.1046/j.1365-3091.2001.00412.x>, 2001.
- 1394 Rosales, I., Quesada, S. and Robles, S.: Paleotemperature variations of Early Jurassic  
1395 seawater recorded in geochemical trends of belemnites from the Basque-Cantabrian  
1396 basin, northern Spain, *Palaeogeogr. Palaeoclimatol. Palaeoecol.*, 203, 253-275,  
1397 [https://doi.org/10.1016/S0031-0182\(03\)00686-2](https://doi.org/10.1016/S0031-0182(03)00686-2), 2004.
- 1398 Rosales, I., Quesada, S. and Robles, S.: Geochemical arguments for identifying second-  
1399 order sea-level changes in hemipelagic carbonate ramp deposits, *Terra Nova*, 18(4), 233-  
1400 240, <https://doi.org/10.1111/j.1365-3121.2006.00684.x>, 2006.
- 1401 Ruhl, M., Hesselbo, S. P., Hinnov, L., Jenkyns, H. C., Xu, W., Riding, J. B., Storm, M.,  
1402 Minisini, D., Ullmann, C. V. and Leng, M. J.: Astronomical constraints on the duration  
1403 of the Early Jurassic Pliensbachian Stage and global climatic fluctuations, *Earth Planet.*  
1404 *Sc. Lett.*, 455, 149-165, <http://dx.doi.org/10.1016/j.epsl.2016.08.038>, 2016.
- 1405 Sames, B., Wagreich, M., Conrad, C. P. and Iqbal, S.: Aquifer-eustasy as the main driver  
1406 of short-term sea-level fluctuations during Cretaceous hothouse climate phases, *Geol.*  
1407 *Society, London, Sp. Publ.*, 498(1), 9-38, <https://doi.org/10.1144/SP498-2019-105>, 2020.



- 1408 Sarr, A. C., Donnadieu, Y., Laugié, M., Ladant, J. B., Suchéras-Marx, B. and Raisson, F.:  
1409 Ventilation Changes Drive Orbital-Scale Deoxygenation Trends in the Late Cretaceous  
1410 Ocean, *Geophys. Res. Lett.*, 49(19), e2022GL099830,  
1411 <https://doi.org/10.1029/2022GL099830>, 2022.
- 1412 Schneider-Mor, A., Alsenz, H., Ashkenazi-Polivoda, S., Illner, P., Abramovich, S.,  
1413 Feinstein, S., Almogi-Labin, A., Berner, Z. and Püttmann, W.: Paleoceanographic  
1414 reconstruction of the late Cretaceous oil shale of the Negev, Israel: Integration of  
1415 geochemical, and stable isotope records of the organic matter, *Palaeogeogr.*  
1416 *Palaeoclimatol. Palaeoecol.*, 319, 46-57, <https://doi.org/10.1016/j.palaeo.2012.01.003>,  
1417 2012.
- 1418 Sequero, C., Bádenas, B. and Muñoz, A.: Sedimentología y cicloestratigrafía de las  
1419 calizas fangosas de plataforma abierta de la Fm. Río Palomar (Pliensbachense inferior;  
1420 Cuenca Ibérica), *Rev. de la Soc. Geol. de Espana*, 30 (1), 71-84, ISSN: 2255-1379, 2017.
- 1421 Silva, R. L., Duarte, L. V., Comas-Rengifo, M. J., Mendonça Filho, J. G. and Azerêdo,  
1422 A. C.: Update of the carbon and oxygen isotopic records of the Early–Late Pliensbachian  
1423 (Early Jurassic, ~187 Ma): Insights from the organic-rich hemipelagic series of the  
1424 Lusitanian Basin (Portugal), *Chem. Geol.*, 283(3-4), 177-184,  
1425 <https://doi.org/10.1016/j.chemgeo.2011.01.010>, 2011.
- 1426 Steffen, K., Thomas, R.H., Rignot, E., Cogley, J.G., Dyurgerov, M.B., Raper, S.C.B.,  
1427 Huybrechts, P. and Hanna, E.: Cryospheric contributions to sea level rise and variability,  
1428 in: *Understanding sea level rise and variability*, edited by Church, J.A., Woodworth, P.L.,  
1429 Aarup, T. and Wilson, W.S., Wiley-Blackwell, Chichester, 177–225,  
1430 <https://doi.org/10.1002/9781444323276.ch7>, 2010.
- 1431 Storm, M. S., Hesselbo, S. P., Jenkyns, H. C., Ruhl, M., Ullmann, C. V., Xu, W., Leng,  
1432 M. J., Riding, J. B. and Gorbanenko, O.: Orbital pacing and secular evolution of the Early  
1433 Jurassic carbon cycle, *P. Natl. Acad. Sci. USA*, 117, 3974–3982,  
1434 <https://doi.org/10.1073/pnas.1912094117>, 2020.
- 1435 Suan, G., Van De Schootbrugge, B., Adatte, T., Fiebig, J. and Oschmann, W.: Calibrating  
1436 the magnitude of the Toarcian carbon cycle perturbation, *Paleoceanography*, 30(5), 495-  
1437 509, <https://doi.org/10.1002/2014PA002758>, 2015.
- 1438 Suárez Ruiz, I and Prado, J.G.: Estudio microscópico de la materia orgánica en las  
1439 pizarras bituminosas del Lías en el litoral de Cantabria, *Acta Geológica Hispánica*, 21-  
1440 22, 585-591, ISSN 1695-6133, 1987.
- 1441 Swart, P. K.: The geochemistry of carbonate diagenesis: The past, present and future,  
1442 *Sedimentology*, 62(5), 1233-1304, <https://doi.org/10.1111/sed.12205>, 2015.
- 1443 Swart, P.K., Blättler, C.L., Nakakuni, M., Mackenzie, G.J., Betzler, C., Eberli, G.P.,  
1444 Reolid, J., Alonso-Garcia, M., Slagle, A.L., Wright, J.D., Kroon, D., Reijmer, J.J.G., Mee,  
1445 A.L.H., Young, J.R., Alvarez-Zarikian, C.A., Bialik, O.M., Guo, J.A. and Haffe, S.:



- 1446 Cyclic anoxia and organic rich carbonate sediments within a drowned carbonate platform  
1447 linked to Antarctic ice volume changes: Late Oligocene-early Miocene Maldives, Earth  
1448 Planet. Sci. Lett., 521, 1-13, <https://doi.org/10.1016/j.epsl.2019.05.019>; 2019.
- 1449 Torrence, C. and Compo, G.P.: A practical guide to wavelet analysis, Bull. Am. Meteorol.  
1450 Soc., 79, 61-78, <https://doi.org/10.1175/1520-0477>, 1998.
- 1451 Tribovillard, N., Algeo, T. J., Lyons, T. and Riboulleau, A.: Trace metals as paleoredox  
1452 and paleoproductivity proxies: an update, Chem. geol. 232(1-2), 12-32,  
1453 <https://doi.org/10.1016/j.chemgeo.2006.02.012>, 2006.
- 1454 Tucker, M. E., Gallagher, J. and Leng, M. J.: Are beds in shelf carbonates millennial-  
1455 scale cycles? An example from the mid-Carboniferous of northern England.... Sediment.  
1456 Geol., 214(1-4), 19-34, <https://doi.org/10.1016/j.sedgeo.2008.03.011>, 2009.
- 1457 Tyson, R.V.: The “productivity versus preservation” controversy; cause, flaws, and  
1458 resolution, in: Deposition of Organic-Carbon-Rich Sediments: Models, Mechanisms, and  
1459 Consequences, edited by: Harris, N.B., Society for Sedimentary Geology (SEPM-SSG),  
1460 Special Publication, 82, 17–33, <https://doi.org/10.2110/pec.05.82.0017>, 2005.
- 1461 Ullmann, C. V., Szűcs, D., Jiang, M., Hudson, A. J. and Hesselbo, S. P.: Geochemistry  
1462 of macrofossil, bulk rock and secondary calcite in the Early Jurassic strata of the Llanbedr  
1463 (Mochras Farm) drill core, Cardigan Bay Basin, Wales, UK, J. Geol. Soc., 179(1),  
1464 jgs2021-018, <https://doi.org/10.1144/jgs2021-018>, 2022.
- 1465 Val, J., Bádenas, B., Aurell, M. and Rosales, I.: Cyclostratigraphy and chemostratigraphy  
1466 of a bioclastic storm-dominated carbonate ramp (late Pliensbachian, Iberian Basin),  
1467 Sediment. Geol., 355, 93-113, <https://doi.org/10.1016/j.sedgeo.2017.04.007>, 2017.
- 1468 Van Mooy, B. A., Keil, R. G. and Devol, A. H.: Impact of suboxia on sinking particulate  
1469 organic carbon: Enhanced carbon flux and preferential degradation of amino acids via  
1470 denitrification, Geochim. Cosmochim. Acta, 66(3), 457-465,  
1471 [https://doi.org/10.1016/S0016-7037\(01\)00787-6](https://doi.org/10.1016/S0016-7037(01)00787-6), 2002.
- 1472 Wang, P.: Global monsoon in a geological perspective, Chin. Sci. Bull., 54, 1113–1136,  
1473 <https://doi.org/10.1007/s11434-009-0169-4>, 2009.
- 1474 Wendler, J. E. and Wendler, I.: What drove sea-level fluctuations during the mid-  
1475 Cretaceous greenhouse climate?, Palaeogeogr. Palaeoclimatol. Palaeoecol., 441, 412-  
1476 419, <http://dx.doi.org/10.1016/j.palaeo.2015.08.029>, 2016.
- 1477 Westphal, H.: Limestone–marl alternations as environmental archives and the role of  
1478 early diagenesis: a critical review, International Journal of Earth Sciences, 95, 947-961,  
1479 DOI 10.1007/s00531-006-0084-8, 2006.
- 1480 Wignall, P. B.: Model for transgressive black shales?, Geology, 19(2), 167-170,  
1481 <https://doi.org/10.1130/0091-7613>, 1991.



- 1482 Woodard, S. C., Thomas, D. J., Hovan, S., Röhl, U. and Westerhold, T.: Evidence for  
1483 orbital forcing of dust accumulation during the early Paleogene greenhouse, *Geochem.*  
1484 *Geophys.*, 12(2), <https://doi.org/10.1029/2010GC003394>; 2011.
- 1485 Zhang, R., Jin, Z., Li, M., Gillman, M., Chen, S., Liu, Q., Wei, R. and Shi, J.: Long-term  
1486 periodicity of sedimentary basins in response to astronomical forcing: Review and  
1487 perspective, *Earth Sci. Rev.*, 104533, <https://doi.org/10.1016/j.earscirev.2023.104533>,  
1488 2023.
- 1489 Zhao, M.Y. and Zheng, Y.F.: Marine carbonate records of terrigenous input into  
1490 Paleotethyan seawater: geochemical constraints from Carboniferous limestones,  
1491 *Geochim. Cosmochim. Acta*, 141, 508-531, <https://doi.org/10.1016/j.gca.2014.07.001>,  
1492 2014.
- 1493